

Computer-aided Detection of Prostate Cancer with MRI: Technology and Applications

Lizhi Liu, MD, Zhiqiang Tian, PhD, Zhenfeng Zhang, MD, PhD, Baowei Fei, PhD

Abbreviations and Acronyms

T2W
T2-weighted
ADC
apparent diffusion coefficient
DCE
dynamic contrast-enhanced
MRS
magnetic resonance spectroscopy
DWI
diffusion-weighted imaging
SVM
support vector machine
AUC
area under a receiver operating characteristic curve
TZ
transition zone
PZ
peripheral zone

One in six men will develop prostate cancer in his lifetime. Early detection and accurate diagnosis of the disease can improve cancer survival and reduce treatment costs. Recently, imaging of prostate cancer has greatly advanced since the introduction of multiparametric magnetic resonance imaging (mp-MRI). Mp-MRI consists of T2-weighted sequences combined with functional sequences including dynamic contrast-enhanced MRI, diffusion-weighted MRI, and magnetic resonance spectroscopy imaging. Because of the big data and variations in imaging sequences, detection can be affected by multiple factors such as observer variability and visibility and complexity of the lesions. To improve quantitative assessment of the disease, various computer-aided detection systems have been designed to help radiologists in their clinical practice. This review paper presents an overview of literatures on computer-aided detection of prostate cancer with mp-MRI, which include the technology and its applications. The aim of the survey is threefold: an introduction for those new to the field, an overview for those working in the field, and a reference for those searching for literature on a specific application.

Key Words: Prostate cancer; MR imaging; image quantification; computer-aided detection.

© 2016 The Association of University Radiologists. Published by Elsevier Inc. All rights reserved.

INTRODUCTION

Prostate cancer (PCa) is currently the most common cancer in men and the second leading cause of cancer-related deaths among men in the United States (1). In 2015, it is estimated that the number of estimated new cases and deaths will be 220,800 and 27,540, respectively,

accounting for 26.0% of new cancer cases and 8.8% of cancer deaths for American men (1).

The prostate is subdivided into the base, mid-gland, and apex from superior to inferior. The prostate also has four anatomic zones: the transition zone (TZ), which contains 5% of the glandular tissue and accounts for around 25% of PCa; the central zone, which contains 20% of the glandular tissue and accounts for around 5% of PCa; the peripheral zone (PZ), which contains 70–80% of the glandular tissue and accounts for about 70% of PCa; and the non-glandular anterior fibromuscular stroma. Accurate localization of PCa within the TZ or the PZ is extremely important as TZ PCa is associated with favorable pathologic features and better recurrence-free survival (2).

At present, the clinical standard for definitive diagnosis of PCa is transrectal ultrasound (TRUS)-guided sextant or systematic biopsy. The prostate-specific antigen (PSA) blood test and digital rectal examination (DRE) results are considered to identify patients who need biopsy. The actual impact of magnetic resonance imaging (MRI) for PCa management is

Acad Radiol 2016; 23:1024–1046

From the Department of Radiology and Imaging Sciences, Emory University School of Medicine, 1841 Clifton Road NE, Atlanta, GA 30329 (L.L., Z.T., B.F.); Center of Medical Imaging and Image-guided Therapy, Sun Yat-sen University Cancer Center, State Key Laboratory of Oncology Collaborative Innovation Center for Cancer Medicine, 651 Dongfeng Road East, Guangzhou, 510060, China (L.L., Z.Z.); Department of Biomedical Engineering, Emory University and Georgia Institute of Technology (B.F.); Winship Cancer Institute of Emory University, 1841 Clifton Road NE, Atlanta, Georgia 30329 (B.F.). Received August 8, 2015; revised March 18, 2016; accepted March 21, 2016. L. Liu and Z. Tian had equal contributions to this work. **Address correspondence to:** B.F. e-mail: bfei@emory.edu

© 2016 The Association of University Radiologists. Published by Elsevier Inc. All rights reserved.
<http://dx.doi.org/10.1016/j.acra.2016.03.010>

through guided biopsies and improved cancer diagnosis and staging yield. In recent years, MRI-targeted prostate biopsies have been showing better disease localization and more accurate sampling than conventional TRUS-guided biopsy in various studies (3–6). MRI-based computer-assisted sophisticated imaging for individual patients would offer such a significant role in defining an optimal targeted biopsy and interventional approach. Several approaches have been explored to improve the accuracy of image-guided targeted prostate biopsy, including in-bore MRI-guided, cognitive fusion, and MRI/TRUS fusion-guided biopsy (7).

MRI provides excellent soft-tissue contrast and has become an imaging modality of choice for localization of prostate tumors. Multiparametric MRI (mp-MRI) includes high-resolution T2-weighted (T2W) MRI, diffusion-weighted imaging (DWI), dynamic contrast-enhanced imaging (DCE-MR), and MR spectroscopy (MRS). The mp-MRI has proven to be an effective technique to localize high-risk PCa (8,9). The combined use of anatomic and functional information provided by the multiparametric approach increases the accuracy of MRI in detecting and staging PCa (8,9). It can also help guide biopsies to achieve a higher tumor detection rate and better reflect the true Gleason grade. The European Society of Urogenital Radiology in 2012 established the Prostate Imaging Reporting and Data System (PI-RADS) scoring system for mp-MRI of the prostate (10). The MR PI-RADS aims to enable consistent interpretation, communication, and reporting of prostate mp-MRI findings (10,11). A joint steering committee formed by the American College of Radiology, European Society of Urogenital Radiology, and the AdMeTech Foundation has recently announced an updated version of the proposals of PI-RADS Version 2 (12). Prostate mp-MRI at 3 T had been recommended in PI-RADS Version 2. Generally, computer-aided detection (CAD) systems are classified into two categories: CAD and computer-aided diagnosis (CADx) systems. Currently, most CAD systems in prostate MRI focus on local suspicious lesions and discrimination between benign and malignant lesions; most of them are CADx systems. As the combination of various MR images creates large amounts of data, supportive techniques or tools, such as CADx, are needed to make a clinical decision in a fast, effective, and reliable way.

In the past 10 years, computer-aided techniques have developed rapidly. Automated CAD and diagnosis may help improve diagnostic accuracy of PCa, and reduce interpretation variation between and within observers (13,14). PCa diagnosis requires an experienced radiologist to read prostate MRI, and such expertise is not widely available. Addition of CADx may significantly improve the performance of less-experienced observers in PCa diagnosis. When less-experienced observers used CADx, they had a similar performance as those experienced observers in distinguishing benign from malignant lesions (13). In a more recent study, the use of CAD can also improve prostate mp-MRI study interpretation in experienced readers (15). For cases in which radiologists are less confident, they can get higher performance by using the

computer output. A recent study showed that a pattern recognition system enables radiologists to have a lower variability in diagnosis, decreases false-negative rates, and reduces the time to recognize and delineate structures in the prostate (16). The benefit of CADx also includes guiding biopsy using cancer location information from MRI (14). Therefore, along with rapid development of MR technique, CADx of PCa has become an active field of research in the last 5 years.

This paper starts with the review of MR image acquisition technology and then focuses on a comprehensive review of the state-of-the-art image quantification methods. The part on validation and clinical applications is a reference of the literatures available in the clinical management of the disease. The paper closes with a discussion and future perspectives.

A PubMed electronic database search for the terms “computer-aided,” “CAD,” “prostate,” and “MRI” was completed for articles about CAD of PCa up to September 11, 2015.

MR IMAGE ACQUISITIONS

Contemporary MRI of the prostate combines anatomic images from high-resolution T1-weighted and T2W sequences and functional information obtained from DWI, DCEI, and MRS. The combination of conventional anatomic and functional MRI is known as mp-MRI. The PI-RADS Prostate MR Guidelines published in 2012 suggest the use of T2W images plus two functional techniques (10). The anatomy of the prostate gland is visualized with T2W images; DWI and MRS add specificity to lesion characterization, whereas DCE-MRI has a high sensitivity in cancer detection. In PI-RADS v2, the essential components of the mp-MRI prostate examination are T2W, DWI, and DCE (12). For the PZ, DWI is the primary determining sequence. For the TZ, T2W is the primary determining sequence. To obtain high and stable accuracy, a combination of anatomic and functional imaging is necessary in clinical practice. Recent studies showed an increasing interest in developing CADx systems to detect and characterize PCa on the basis of an mp-MRI approach (14,15,17,18). T2W-MR images are frequently used in mp-MRI CADx systems. T2W plus DWI and DCE-MRI are also commonly used among the combinations.

T2WI and T2 Mapping

The anatomy of the prostate gland is best visualized with T2W images. The acquisition of high-resolution T2W images of the prostate is the first and most important step in an mp-MRI protocol. In T2W images, the PZ of the prostate has hyperintense signal, whereas the central zone and TZ have low signal, allowing the zonal anatomy of the prostate to be clearly delineated (Fig 1). In T2W images (Fig 2), PCa in the PZ is usually depicted as a low-signal area. However, the growth pattern and the aggressiveness of the tumor can alter its appearance. T2W-MRI has been advocated as an accurate technique in the detection of PCa in the TZ (19,20).

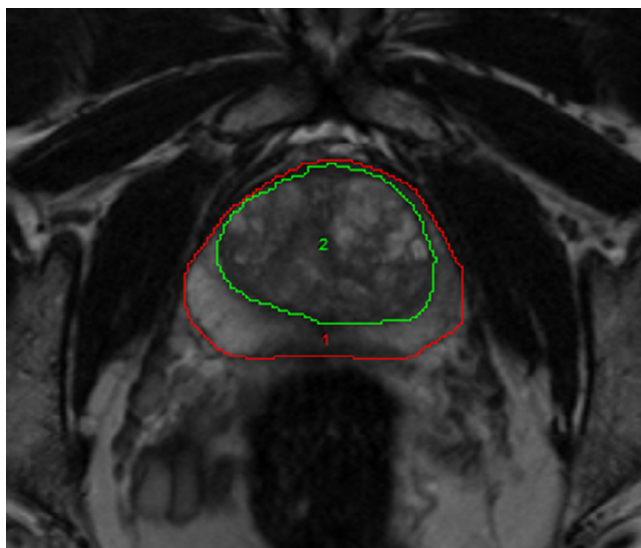


Figure 1. High-resolution T2-weighted magnetic resonance imaging (MRI). T2-weighted MR images can differentiate the normal intermediate- to high-signal-intensity peripheral zone (region 1) from the low-signal-intensity central and transition zones (region 2).

The value of T2W-MR images is also in predicting pathologic stage and extracapsular extension of PCa (21).

Because T2W-MR images play an important role in both location and staging of PCa, T2W-MRI is the most frequently used sequence in CADx systems for PCa. In T2W-MR images, the tumor region of interest (ROI) has more dark pixels than bright pixels, whereas the normal tissue ROI has more bright pixels than dark pixels. Different features, including fractal features, textural features, and signal intensity, can be used by CADx. Because PCa at the central gland and PZ usually have significantly different texture on T2W-MR images (22), and because the use of mp-MRI may have challenges for detecting cancer at the TZ (23), a CADx system that can analyze features based on the lesion's location may be able to aid in the detection of suspicious lesions.

T2 maps offer quantitative T2 values. As the standard T2 mapping approach of performing multiple single spin-echo acquisitions with a range of echo time (TE) settings requires excessive scan times, the T2 mapping is not included in most clinical applications. Recently, some new sequences can provide an effective approach to speed up T2 quantification (24-26). T2 values of histologically proven malignant tumor areas were significantly lower than the suspicious but nonmalignant lesions or normal areas (24). The use of quantitative T2 measurement improves the specificity and/or sensitivity of PCa detection (27) and aggressiveness assessment (28,29). There is a potential benefit of incorporating quantitative T2 values into CADx systems.

DCE-MRI

DCE-MRI, which enables visualization of vascular permeability and perfusion, is an important tool in oncology to define

tumor. DCE-MRI is sensitive to alterations in vascular permeability, extracellular space, and blood flow. The clinical application of DCE-MRI for PCa is based on data showing that malignant lesions show earlier and faster enhancement and earlier contrast agent washout compared to healthy prostate tissues (Fig 3) (30).

The DCE-MRI data can be analyzed with various semiquantitative or quantitative models to extract parameters related to vascular permeability, extracellular space, blood flow, and water exchange (31). As semiquantitative DCE-MRI data are relative only to the patient, the baseline intensity is highly variable depending on the patient and the MRI protocol. It is necessary to use indicators relating to signal amplitude. The most commonly used quantitative approach of analyzing DCE-MRI is two-compartment pharmacokinetic (PK) models that can be used to generate PK parameters such as K^{trans} (transfer of gadolinium contrast from the vasculature to the tumor, representing forward vascular perfusion and permeability) and K^{ep} (reverse transfer of contrast agent from the extracellular space back to the plasma, representing backward leakage) to quantify tumor enhancement and the contrast uptake and washout (32). However, PK model implementation typically involves assuming some prior knowledge, and the arterial input function estimation methodology can have significant effects on the parameters estimated by PK modeling (33). The empirical approach based on phenomenological universalities is able to reproduce experimental data from a DCE-MRI acquisition (34,35).

Different CADx systems have been developed to analyze the DCE-MRI data. Vos et al. developed a CADx system capable of discriminating PCa from nonmalignant disorders in the PZ and achieved a diagnostic accuracy of 0.83 (0.75-0.92) (36). They also developed an automated segmentation per patient calibration method to improve the diagnostic accuracy of CADx (37). Puech et al. designed a prostate CADx software to provide a five-level cancer suspicion score for suspicious foci detected in DCE-MRI and T1-weighted images (38,39).

DCE-MRI usually has lower spatial resolution than other sequences, especially when DCE-MRI is performed rapidly in a short period of time. Limitations in the interpretation of DCE-MRI data include overlap in enhancement properties between benign and malignant regions in the TZ. Benign prostatic hyperplasia and other benign inflammatory conditions within the TZ also exhibit substantial hypervascularity (40). Diagnostic models containing contrast-enhancement parameters have reduced performance when applied across zones, so zone-specific models can improve classification of PCa on mp-MRI (41).

Diffusion-weighted MRI

The diffusion properties of tissue are related to the amount of interstitial free water and permeability. In general, cancer tends to have more restricted diffusion than normal tissue, because of the higher cell densities and abundance of

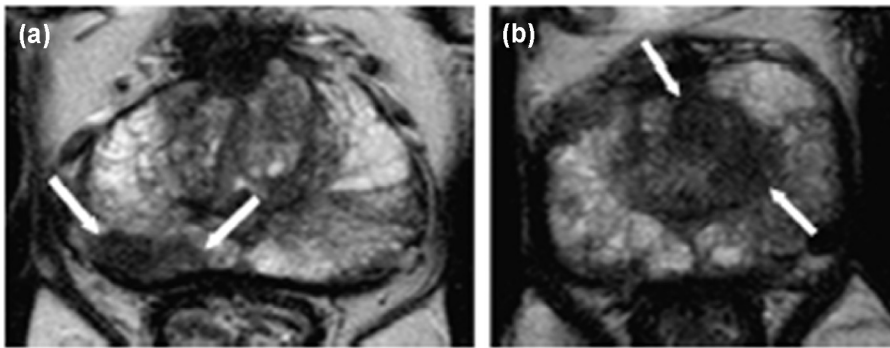


Figure 2. High-resolution T2-weighted magnetic resonance (MR) images of prostate cancer. **(a)** There is a low-signal intensity lesion on the right peripheral zone (*white arrows*) at the mid-gland of the prostate. At prostatectomy, the lesion was classified as a Gleason grade 7 (4 + 3) prostate adenocarcinoma. **(b)** An ill-defined homogeneous low-signal-intensity area at the left transition zone (*white arrows*) at mid-gland of the prostate in another patient. Transrectal ultrasound (TRUS)-guided biopsy showed a Gleason grade 8 (4 + 4) prostate adenocarcinoma on the corresponding position (images from Reference (53)).

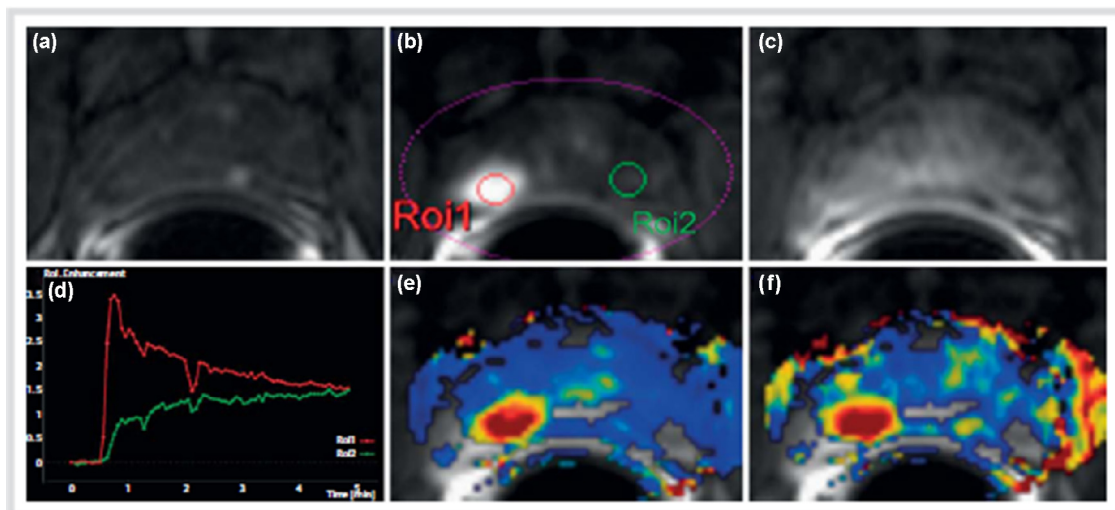


Figure 3. Dynamic contrast-enhanced magnetic resonance imaging (MRI) (dynamic contrast-enhanced imaging [DCE-MRI]) of the prostate. **(a)** Axial T1 gradient echo (GRE) sequence unenhanced image. After contrast agent administration, an area with early enhancement is seen on the right in the peripheral zone **(b)**, region of interest [ROI1] with significant washout in the late-phase image **(c)**. The curve (*red*) with early enhancement is a typical finding in the case of prostate cancer, whereas healthy prostate tissue is characterized by a steady slow enhancement (*green*). High transport constants K^{trans} **(e)** and k^{ep} **(f)** can confirm suspicion of prostate cancer. Prostate adenocarcinoma with a Gleason score of 4 + 5 = 9 was diagnosed after prostatectomy (image from Reference (30)). (Color version of figure is available online.)

intra- and intercellular membranes in cancer (42). Diffusion-weighted MRI images can be used to detect PCa from differences in the diffusion of water molecules of the normal and tumor tissues (Fig 4) (42). The DWI is usually generated with different b-values that can be used to calculate the apparent diffusion coefficient (ADC), and the ADC for each pixel of the image is displayed as an ADC map. Diffusion of water molecules in tumor tissue is thought to reflect tissue architecture such as cell density and nucleus-to-cytoplasm ratio, and reductions in ADC values. For these reasons, ADC values have received the attention as a predictor of Gleason score in PCa (43,44). Studies show that DWI findings may indicate tumor aggressiveness (27,45,46).

Technologic advances enable performance of DWI at high b- or ultrahigh b-values (greater than 1000 s/mm²). High b-value images can be obtained in one of two ways: either

directly by acquiring a high b-value DWI sequence, or by calculating (synthesizing) the high b-value image by extrapolation from the acquired lower b-value data. Previous research has shown that high b-value DWI images allow for increased delineation between tumors and healthy tissue, which makes the PCa detection more robust (47,48). Whereas contrast in ADC maps does not significantly change with different b-values, contrast ratios of DWI images are significantly higher at b-values of 1500 and 2000 s/mm² in comparison to b-values of 800 and 1000 s/mm² (49). Wang et al. have reported that DWI images and ADC maps using b = 1500 s/mm² should be considered more effective than those at b = 2000 s/mm² or b = 1000 s/mm² for detecting PCa at 3 T MRI (50).

DWI images and ADC maps are the key component of the prostate mp-MRI examination. Several CADx systems adopting DWI images or ADC maps have been developed.

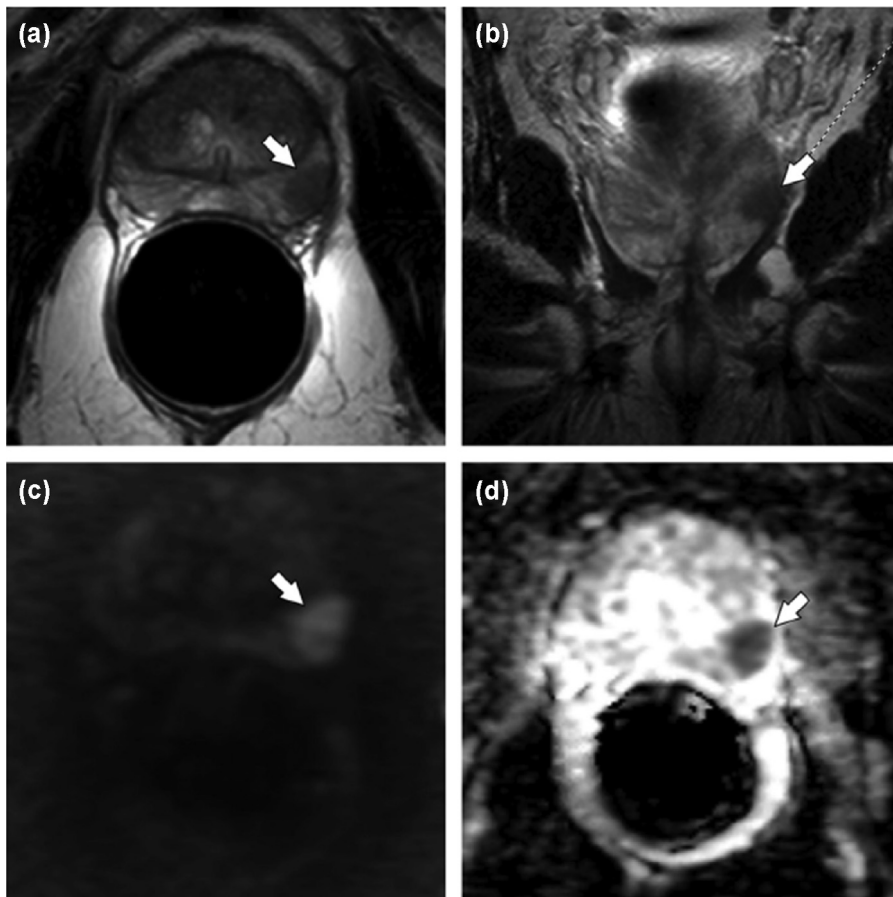


Figure 4. Multiparametric MRI (mp-MRI) of the prostate. Axial T2 turbo spin echo (TSE) (a) and coronal T2 TSE (b) images show a well-defined T2 hypointense lesion in the peripheral zone (arrow) with corresponding high signal on diffusion-weighted imaging (DWI) (c) and low signal on the apparent diffusion coefficient (ADC) map (d). Biopsy of this region was positive for Gleason 4 + 3 prostate cancer (images from Reference (42)).

DWI was mostly often combined with T2W in these CADx systems. Peng et al. demonstrated that the combination of 10th percentile ADC, average ADC, and T2W skewness with CADx is promising in the differentiation of PCa from normal tissue (27). Niaf et al. presented a CADx system based on T2W, DWI, and DCE to assist cancer identification in the PZ (18). Stember et al. developed a software system that identifies suspicious regions at the prostate TZ using signal and textural features on T2W and ADC maps, free of user input (51). Kwak et al. recently designed a prostate CADx combined T2W and high b-value ($b = 2000 \text{ s/mm}^2$) DWI. They obtained an area under a receiver operating characteristic curve (AUC) of 0.89 (52).

MRS

In MRS, the position of each metabolite peak in the output graph reflects the resonant frequencies or chemical shifts of its hydrogen protons, and the area of each peak reflects the relative concentration of that metabolite (53). The dominant peaks observed in prostate MRS are from protons in citrate (2.60 ppm), creatine (3.04 ppm), and choline compounds (3.20 ppm) (Fig 5) (53).

As a metabolic biomarker for PCa, MRS has not gained wide acceptance in routine clinical practice owing to a variety of factors including the length and complexity of data acqui-

sition, zonal anatomy, processing, and analysis. Visual interpretation of the spectra by a trained spectroscopist is time-consuming and requires accurate knowledge of prostate anatomy. Therefore, a method for automated analysis of prostate MRS data is necessary.

Over the last decade, with a view on assisting radiologists in interpretation and analysis of MRS data, several researchers have begun to develop CADx schemes for PCa identification from spectroscopy. Tiwari et al. developed an approach that integrated a manifold learning scheme (spectral clustering) with an unsupervised hierarchical clustering algorithm to identify spectra corresponding to cancer on prostate MRS (54). The scheme successfully identified MRS cancer voxels with a sensitivity of 77.8%, a false-positive rate of 28.92%, and a false-negative rate of 20.88% (54). They also presented a CADx scheme that integrated nonlinear dimensionality reduction with an unsupervised hierarchical clustering algorithm to automatically identify suspicious regions on the prostate using MRS (55). They introduced the use of wavelet embedding to map MRS and T2W texture features into a common space to identify the voxels that are affected by PCa (56). They recently presented a computerized decision support system called Semi Supervised Multi Kernel Graph Embedding that may be developed into a powerful diagnostic and prognostic tool for distinguishing high- and low-grade PCa in vivo. Matulewicz et al. used an artificial neural network

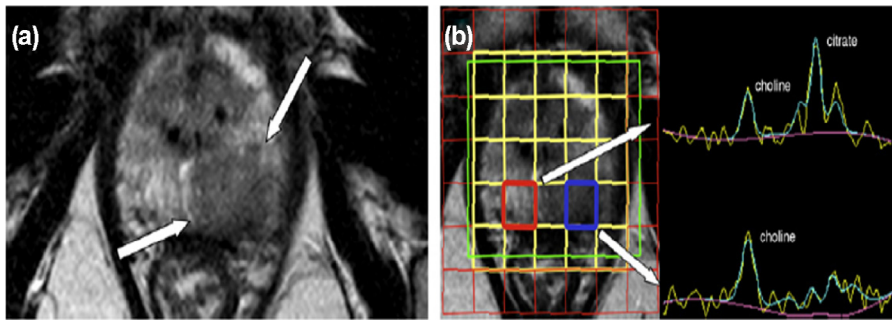


Figure 5. Magnetic resonance spectroscopy (MRS) of prostate cancer. **(a)** Axial T2-weighted MR images at the level of the prostate mid-gland to apex shows a large hypointense lesion on the left peripheral zone. **(b)** A three-dimensional (3D) MRS shows a normal spectrum on the right peripheral zone (*red box*) with normal choline plus creatine-to-citrate ratio of 0.48. In the voxel placed over the lesion on the left peripheral zone (*blue box*), the curve shows an increased choline peak and the citrate peak is markedly reduced. Random systematic biopsy showed a Gleason grade 9 (4 + 5) prostate adenocarcinoma on the left apex (images from Reference (53)). (Color version of figure is available online.)

model to automatically detect cancerous voxels from prostate MRS datasets and found that the additional information concerning the prostate's zonal anatomy can improve the performance of the detection (57).

Other Imaging Methods

Although T2W, DWI, DCE-MRI, and MRS are more commonly used in mp-MRI, some MRI methods, including diffusion tensor imaging (DTI), diffusion kurtosis imaging (DKI), and MR elastography (MRE), have been investigated for the characterization of PCa (58–61). Other MRI methods, including proton density-weighted image (62) and T1 map (14), had also been added for feature calculation purposes in some CADx systems.

DTI has been widely used in clinical applications, especially in neuro- and musculoskeletal imaging. Fractional anisotropy and ADC values provided from DTI data reflect the degree of water diffusion restriction in different tissues. Pathologic processes may cause a change in normative fractional anisotropy values and disruption of fibers in tractography. The feasibility of performing DTI of the prostate had been demonstrated by some studies, and DTI tractography can successfully visualize fiber tracts around the prostate (58). DTI tractography might be applicable to the estimation of structures of the prostate (59), the characterization of PCa (60), and monitoring prostatic structural changes under radiotherapy (61).

The novel technique, DKI, enables characterization of non-Gaussian water diffusion behavior. DK model may add value in PCa detection and diagnosis, and DKI potentially offers a new metric for assessment of PCa (63). A recent study demonstrated no significant benefit of DKI for detection and grading of PCa as compared to standard ADC in the PZ determined from b-values of 0 and 800 s/mm (64). The mechanical properties of the tissue of interest are calculated from the wave fields and displayed as an image, commonly referred to as an elastogram. In MRE, an external mechanical excitation is applied to the tissue of interest to induce tissue vibrations (65). MRE has been shown to be of clinical value in MRI for its

ability to detect tissue abnormalities in organs such as the liver (66), brain (67), and breast (68–70). More recently, researchers have also focused on the development of MRE methods to detect PCa (71–73). The resulting wave fields are imaged using a motion-sensitized MRI pulse sequence. Elastograms may add another dimension to current mp-MRI techniques for diagnosis of PCa, and may further increase the sensitivity and specificity of such techniques.

T1 maps offer quantitative T1 values and can be produced by a variety of methods, such as multiple inversion or multiple repetition time acquisitions, typically requiring lengthy acquisition times. Another approach taken in the context of the prostate has been to employ spoiled gradient echo sequences where it is possible to obtain T1 estimates in relatively short acquisition times by varying the radiofrequency (RF) flip angle (74). The T1 mapping is not included in most CADx systems. Vos et al. (14) had presented a fully automatic CADx by combining a histogram analysis on mp-MR images including T1, PK, T2, and ADC maps.

MR lymphography has been used for the investigation of the lymphatic channels and lymph glands. Different imaging techniques, including nanoparticle-enhanced (75,76) and non-contrast MR lymphography (77,78), had been developed for detection of nodal metastases. MR lymphography is a non-invasive technique that is well suited for the examination of regional (intrapelvic) lymph node metastases in PCa.

MR IMAGE QUANTIFICATION METHODS

General Framework

Development of CAD systems includes several aspects: image preprocessing, algorithm development, methodology for CADx performance assessment, validation using appropriate cases to measure performance and robustness, observer performance studies, performance assessment with a clinical trial, and ultimately, commercialization. The development must confront several challenges. Computerized image procedure may cover different aspects of segmentation, registration, feature extraction, and classifiers. A computer algorithm should be developed

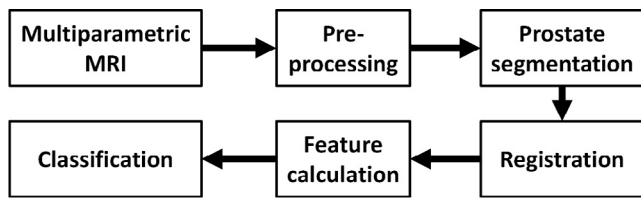


Figure 6. Flowchart for computer-aided detection of prostate cancer in multiparametric magnetic resonance imaging (mp-MRI).

based on the understanding of image reading by radiologists, such as how radiologists detect certain lesions, why they may miss some abnormalities, and how they can distinguish between benign and malignant lesions. It is important to develop CADx systems that extract quantitative data in a more accurate and automated fashion.

Many different types of CADx systems are produced to locate/diagnose PCa in MRI, including T2W, DWI, DCE-MRI, and MRS. Considering the particularity of PCa in anatomy, pathology, and clinic, the core of a CADx system for the detection of PCa is associated with its computerized algorithms. In general, the pipeline of the CADx system for PCa is visualized schematically in Figure 6. In the initial stage, lesion candidates are selected within a likelihood map that is generated by a voxel classification of one or more images. Hereafter, the lesion candidates are segmented into a ROI from which region-based features are extracted. Finally, the extracted information is fused by a classifier into malignancy likelihood. The following sections describe each step in detail.

Preprocessing

The purpose of preprocessing is to normalize the MR data or to transform the MR data to a domain in which prostate lesions can be easily detected.

For T2W-MRI, the image intensities can vary, even when using the same protocol and the same scanner. The quality of images depends on the acquisition conditions such as temperature, calibration adjustment, B0 intensity, coil position, and the receiver gain value. In addition, the intensity variation will increase when different scanners are used. This relationship must be taken into account for MR image analysis. Collewet et al. (79) proposed four schemes for the intensity normalization. The most used method is that intensities are proportionally normalized by defining the median + 2* (interquartile range).

ADC maps calculated from DWI are useful for the detection of PCa with a relatively high specificity. However, it has lower resolution than T2W-MRI and is subject to magnetic susceptibility artifacts (17). ADC represents a quantitative assessment of water diffusion. Lower ADC value is associated with higher rate of malignancy. PCa can be identified as a low-signal region on ADC maps against a background of normal tissue with higher signal intensity (17).

Intensity inhomogeneity arises from the imperfections of the image acquisition, which can reduce the accuracy of seg-

mentation, classification, and registration. The most intuitive method to correct intensity inhomogeneity is image smoothing or homomorphic filtering (80). Vovk et al. (81) classify inhomogeneity correction methods into two categories, which are prospective and retrospective. Prospective methods aim at the calibration and improvement of image acquisition processes. Retrospective methods rely exclusively on the information of the acquired images or on a priori knowledge. Sled et al. (82) proposed a nonparametric nonuniform intensity normalization (N3) method for inhomogeneity correction, which is independent of pulse sequence. Tustison et al. (83) proposed a variant of N3 for bias field correction. Similar to the N3, the source code, testing, and technical documentation are publicly available and the package is "N4ITK." This algorithm is available to the public through the Insight Toolkit of the National Institutes of Health.

Segmentation

The segmentation aims to reduce the burden of the classifier in the later stages. Therefore, the classifiers focus only on the prostate region obtained by segmentation methods. T2W imaging provides the best resolution and contrast to show the anatomy of the prostate and has a very high sensitivity for PCa. Therefore, T2W-MRI is the most useful image sequence in determining the contours of the prostate.

Extensive studies were developed to segment the prostate from MR images (62,84–90). It can be a challenging task to obtain accurate prostate volume in T2W-MRI. First, the contrast between the prostate and the surrounding tissues can be low. Therefore, it may be difficult to accurately segment the boundary of the prostate. Second, the prostate shapes of different patients can be significantly different. Even for the same patient, the prostate motion at different patient positions can be large, which results in a shape difference on MR images. Third, MR image appearance, quality, and the presence of artifacts can be affected by different scanners, which in turn can have a large influence on the performance of computerized algorithms. All these aspects need to be considered when developing a robust and accurate segmentation method for prostate MR images.

Contour- and shape-based methods (91–95) exploit edge and shape features to segment the prostate, which contains two categories. The first category is edge-based segmentation methods. The edge detection operators are used to produce edges on MR images. The candidate edges are picked up and then connected to obtain the prostate boundary. Zwiggelaar et al. (91) developed a semiautomatic method to segment the prostate in MRI data. Their method exploits the characteristics of the anatomic shape of the prostate when represented in a polar transform space. The edge detection and non-maximum suppression are used to track the boundary of the prostate.

The second category is deformable model-based segmentation methods. Kass et al. (96) proposed an active contour model and used the image gradient to evolve a curve. The

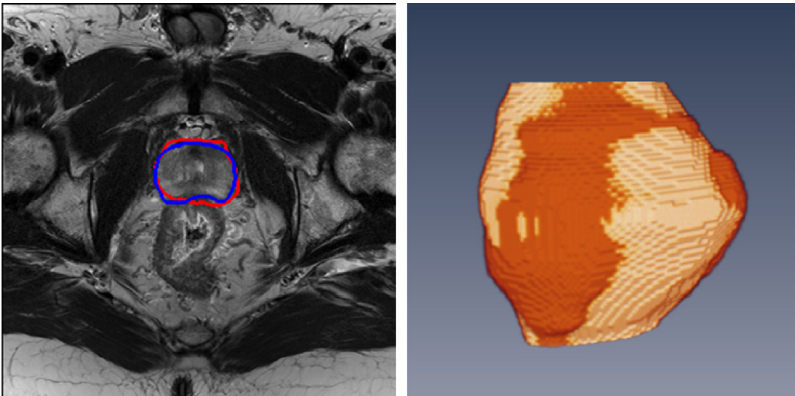


Figure 7. Prostate segmentation on magnetic resonance (MR) images. **Left:** Two-dimensional (2D) MR image and segmentation results where the red curve represents the segmentation from a computer algorithm, whereas the blue curve is the ground truth labeled by a radiologist. **Right:** Three-dimensional (3D) visualization after segmentation. The gold region is the prostate surface obtained by the computer algorithm, whereas the red region is the ground truth. (Color version of figure is available online.)

internal spline force pushes the curve toward the salient image feature, whereas the external force is responsible for putting the curve near the object. Chan and Vese (97) proposed a level set algorithm of the piecewise constant variant of the Mumford-Shah model (98) for segmentation.

Atlas-based methods are also used to segment the prostate in MR images (99). An atlas consists of original image data and its corresponding manual segmentation. The atlas can be used as a reference to segment the prostate of a new patient. Klein et al. (99) proposed an automatic method for the segmentation of the prostate in three-dimensional (3D) MR images. Their method is based on nonrigid registration of a set of pre-labeled atlas images. The label images of the deformed atlas are fused to yield a segmentation of images from a new patient.

Besides the above methods, a global optimization algorithm called graph cut (100,101) is becoming more and more popular owing to its efficient global minimization. The segmentation problem can be formulated as a minimization of an energy minimization. Egger (102) proposed a graph-based approach to automatically segment the prostate based on a spherical template. The minimal cost on the graph is optimized by a graph cut algorithm, which can get the segmentation of the prostate volume. Mahapatra and Buhmann (85) proposed a fully automatic method for prostate segmentation using random forests classifiers and graph cuts. The prostate probability map was generated based on a random forests classifier. The negative log likelihood of the probability maps was used as the penalty cost in an energy function, which was minimized by graph cuts. Tian et al. (103) proposed a supervoxel-based segmentation method for the prostate. The prostate segmentation problem was considered as assigning labels to supervoxels. An energy function with both data and smoothness terms was used to model the labels, which was minimized using graph cuts. The segmentation results are shown in Figure 7. Other segmentation methods were also developed for the prostate (104,105). Ghose et al. (105) reviewed segmentation methods for the prostate in TRUS, MR, and computed tomography (CT) images. They studied the similarities and differences among the different methods, and highlighted their advantages and disadvantages to assist in the

choice of an appropriate segmentation method. They also showed a comprehensive description of the existing methods in all TRUS, MR, and CT images, and highlighted their key points and features. They provided a strategy for choosing segmentation method for a given image modality.

A publicly available data set called Medical Image Computing and Computer Assisted Interventions (MICCAI) Challenge Prostate MR Image Segmentation (104) can be used to evaluate the performances of the new proposed methods. This data set contains 50 cases with ground truths for training, and 30 cases without ground truths for testing, which are 3D T2W-MR transverse images of the prostate. The MR images were obtained from multicenter, multivendor, and different acquisition protocols (ie, with/without endorectal coil [ERC], differences in slice thickness).

Registration

Image registration is a process of aligning two or more images, which aims to find the optimal transformation that best aligns the structures of interest in the input images. Image registration is needed to integrate the features from different images of mp-MRI such as DCE-MRI and T2W-MRI. The registration of images requires the selection of the feature space, a similarity measure, a transformation type, and a search strategy (106). The digital imaging and communication in medicine (DICOM) header of MR images can provide coordination and orientation information that are useful for registering T2W, ADC, and K^{trans} maps. T2W-MRI is considered as the reference. Other modalities can be registered to T2W-MRI by aligning the coordinates of their origins, which are obtained from the DICOM header. If necessary, resolution adjustment is also performed after the alignment.

Registration is also used to validate in vivo MRI using ex vivo histologic images (107,108). To obtain the reliable ground truth of the PCa region, whole-mount histology is performed on ex vivo prostate. The pathologist labels the cancer region in the histology images. Based on the registration between the whole-mount histology and T2W-MRI, the labeling of the cancer in histology can be mapped to T2W-MRI for validation (107,108). Kalavagunta et al. (108) proposed

a method to register MRI and histology using local affine transformations guided by internal structures. First, the histologic and MR images are first segmented, scaled, and translated. Second, the prostate capsule and internal structure masks are identified to constrain the pathology transformation. A transformation matrix is obtained by registering two images based on capsule and internal structure masks. Third, the pathology images are warped using a computed transformation matrix. Fourth, a transformation matrix is applied for each annotated cancer region. The warped cancer regions are superposed on registered pathology images. Last, the cancer regions in MRI can be obtained by mapping the cancer regions of pathologic images to MR images. In another study, Chappelow et al. (107) presented a new registration method that maximizes the combined mutual information shared by the intensity of the reference image and multiple representations of the floating images in multiple feature spaces. The method provides enhanced registration performance by combining the intensity information with transformed feature from the images. These features are not susceptible to intensity artifacts and provide additional information for the registration between the reference and floating images. This method is particularly useful for registering MRI and histology.

Feature Extraction

Feature extraction plays an important role in prostate MRI CADx systems. Classic features for medical images include intensity, shape, texture, and statistical features. For medical image classification, choosing the right features for a classifier is more important than choosing the classifier itself (62).

Litjens et al. classified the features into five types: intensity, PK, texture, blobness, and anatomic features (62). For the intensity feature, a T2-estimate map is generated by using the MR signal equation, the proton density image, and a reference tissue (88). Anatomic features include the relative distance to the prostate boundary and the relative position feature. Both the relative distance and the relative position features are calculated with respect to the prostate surface obtained by segmentation methods. For the PK feature, the traditional analysis is incorporated in their CADx system by using a curve fitting technique to fit a bi-exponential curve to the time data, as presented in Reference (109). For the texture feature, a Gaussian texture bank was used to capture the textural distortions (22). For the blobness feature, it was found that PCa tends to appear as a blob-like lesion in DWI and DCE-MRI. The blobness filter presented by Li et al. was chosen as a blobness measure (110). Blobness is calculated on the ADC, tau, and LateWash images, as well as on the K^{trans} and K^{ep} images (110).

Shah et al. (17) created an mp-MRI feature set for CADx systems (Fig 8). First, to reduce interpatient variability, normalized T2W maps were calculated from the transversal T2W intensities using the average fat signals adjacent to the prostate as the reference. Second, quantitative ADC maps were computed from the transversal DWI by fitting the de-

pendence of the signal intensity in each pixel. Third, each dynamic curve was de-noised by using a wavelet filter for DCE-MRI. The PK parameters were extracted by using the generalized kinetic model (111,112). Then, the generalized kinetic model was fitted to the measured concentration time curves, using the linear least squared method (112) to yield the volume transfer constant K^{trans} and the rate constant k^{ep} . Finally, the normalized T2W and ADC maps were resized to have a pixel resolution equal to the T1 and K^{trans} and k^{ep} maps to form the final feature set for the CADx system.

Niaf et al. extracted about 140 kinds of features for a CADx system (18). Most of these features were chosen based on their proven efficiency between cancer and noncancer. Two categories of features were proposed: image features and functional features. For image features, there were three types: gray-level features, texture features, and gradient features. The image intensity values of T2, DCE, and ADC maps were used as gray-level features. First-order texture measurements were computed for each pixel over a local window, which includes mean, median, standard deviation, and average deviation. Second-order texture features were computed based on two neighboring pixels, which includes co-occurrence matrix. The Sobel and Kirsch filters and numerical gradient operators were used to compute gradient features (Fig 9).

Radiomics is an emerging field for the quantification of tumor phenotypes by applying a large number of quantitative image features (113,114). Radiomics can provide complementary and interchangeable information to improve individualized treatment selection and monitoring. Because medical imaging technology is routinely used in clinical practice worldwide, radiomics may have a high clinical impact on future patient management. The workflow of radiomics consists of three steps (113). The first step is the acquisition of standardized images for diagnostic or planning purposes. On the images, the tumor regions are extracted by an algorithm or by an experienced radiologist. Second, quantitative imaging features are extracted from the tumor regions. These features involve tumor image intensity, texture, and shape and size of the tumor. Last, all the extracted features are analyzed and selected by a model. The most informative features are identified and incorporated into predictive models for treatment outcome. Radiomics, as a high-dimensional mineable feature space, can be used for PCa. Cameron et al. had constructed a comprehensive radiomics feature model to detect tumorous regions using mp-MRI (115). New radiomics-driven texture feature models had been developed for the detection of PCa and for the classification of PCa Gleason scores by using mp-MRI data (116–118).

Classification

Image classification involves training and testing with features extracted from image data and its corresponding labels (62). A classifier is usually trained by using the labeled image data set and applying it to unseen image data sets. Several

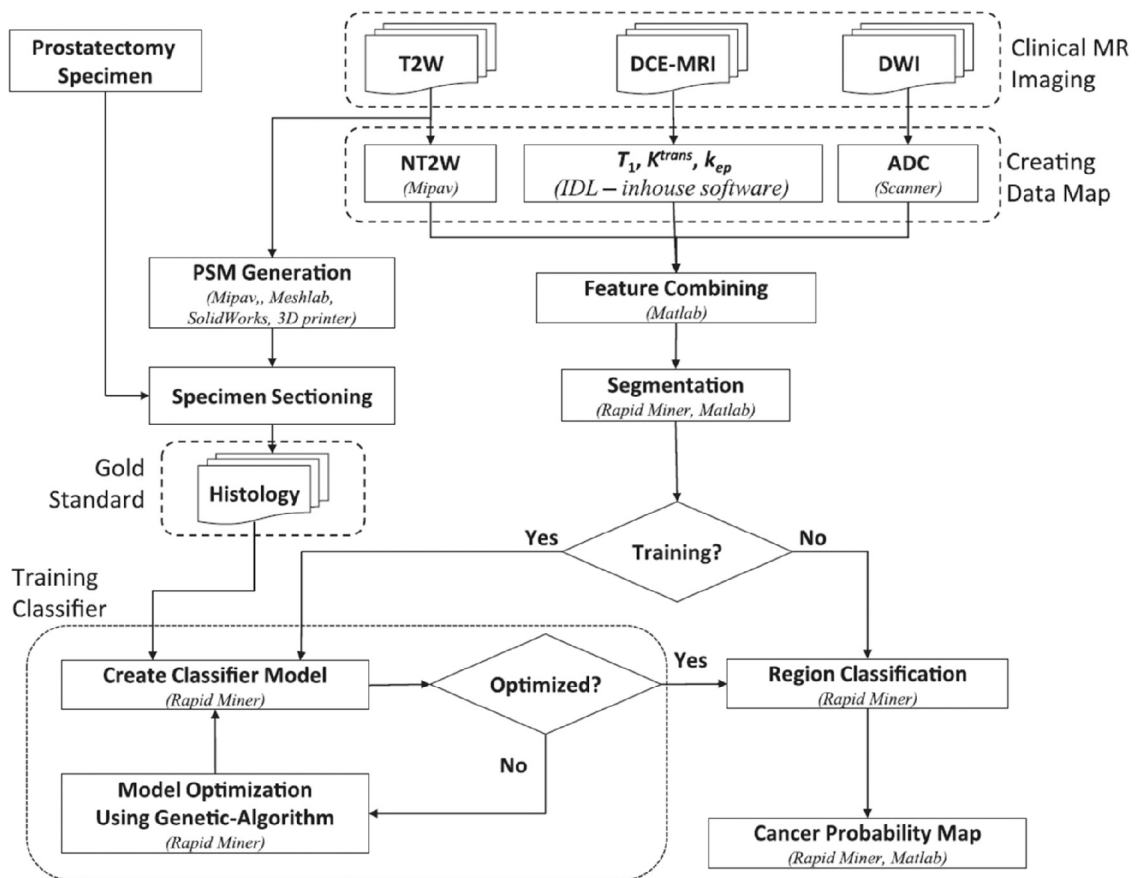


Figure 8. Flowchart for a computer-aided detection (CAD) system based on a multiparametric magnetic resonance imaging (mp-MRI). The cancer probability map is the final outcome of the algorithm (image from Reference (17)).

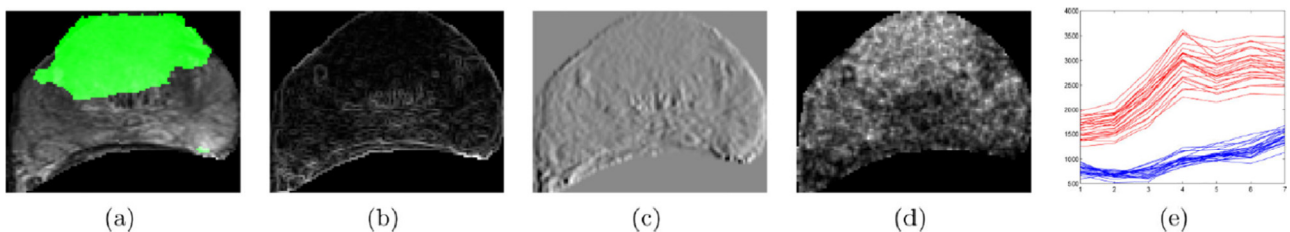


Figure 9. Image features for prostate cancer detection. (a) Prostate cancer superposed in green. (b) First-order statistics (standard deviation). (c) Sobel-Kirsch feature. (d) Second-order statistics (contrast inverse moment). (e) Corresponding time-intensity curves for CaP (red) and benign (blue) regions are shown based on dynamic contrast-enhanced imaging (DCE-MRI) data (images from Reference (129)). (Color version of figure is available online.)

classification techniques from the machine learning field have been developed to pick up discriminative features. Support vector machines (SVMs) and random forests could achieve good performance based on the positive and negative training samples (17,119). A pixel classification provides a likelihood between 0 and 1 for each pixel, with 0 indicating no suspicion of PCa and 1 indicating high suspicion of cancer.

Litjens et al. (62) experimented with three different classifiers: a linear discriminate classifier, a GentleBoost classifier (120), and a random forests classifier (119) with regression trees. Shah et al. used SVM to create a classifier model (17). Because real data are not linearly separable, the SVM implementa-

tion was used to allow relaxed constraint for misclassified points. SVM “kernel trick” was also implemented to enable operations to be performed in the input space rather than in the potentially high-dimensional feature space (121).

Chan et al. (122) investigated the use of a statistical classifier in detecting PCa by combining information from MR images. SVM is used to predict the tumor likelihood in the PZ using the derived features. For SVM training, they randomly sampled 10% of the PZ data and retained all the tumor data to confine the training dataset to a manageable size for SVM training convergence. The radial basis function kernel was used for SVM. These works indicate that the SVM

classifiers and random forests work well on the problem of classifying prostate tumors on mp-MRI.

VALIDATION

The accuracy of the “gold standard” is important when developing a CADx system for prostate MRI. Histopathology, as the ground truth, usually includes findings from prostatectomy specimens or biopsy specimens. The validation of CADx systems is summarized in Table 1. To transfer the labels

from pathology to MR images, MR images usually need to be registered with pathologic sections of the prostate. An accurate registration of histologic and MR images serves as the bridge between in vivo anatomic information and ex vivo pathologic information, which is valuable in developing a CADx system.

Whole-mount sections are generated from tissue slices, and microscopic slices are stained with hematoxylin-eosin after being embedded in paraffin (111,123). Pathologists outline each lesion on the microscopic slices. Gleason scores of different regions may also be provided on the microscopic slices. For

TABLE 1. Validation of CADx Systems

Reference	Ground Truth on the Histology	Candidate on MR Image	Image Registration
Chan et al. (122)	Biopsy	MO	NA
Puech et al. (39)	Needle biopsy or prostatectomy	MO	NA
Tiwari et al. (54)	Biopsy	Sextant location determined by radiologist	NA
Vos et al. (36)	WMHS + MO	MO	3D rendering mode
Viswanath et al. (140)	WMHS + MO	MANTRA	Multimodal image registration
Viswanath et al. (129)	WMHS	MANTRA	Multimodal image registration
Vos et al. (37)	WMHS	Not specified	Not specified
Liu et al. (141)	WMHS + MO	MO + ex vivo MRI	Manual
Tiwari et al. (55)	WMHS + sextant boundaries	A joint review session of trial imagers and pathologists	NA
Artan et al. (142)	WMHS + MO	Tumor location is transferred to the in vivo MRI from histologic images + ex vivo MRI	NA
Vos et al. (143)	WMHS + MO	MO	Mutual information registration
Viswanath et al. (144)	WMHS + MO	Registration from histologic images	MACMI
Lopes et al. (145)	WMHS + drawn by urologists	Drawn by urologists	Manual correspondence
Liu and Yetik (26)	WMHS + MO	MO + ex vivo MRI	Manual registration
Sung et al. (146)	Radical prostatectomy + MO	The radiologist matched the pathologic slices with corresponding MRI	NA
Tiwari et al. (56)	WMHS	MO + ex vivo MRI	Manual registration
Viswanath et al. (22)	WMHS + MO	Registration from histologic images	Multimodal elastic registration
Vos et al. (14)	Needle biopsy	Combining the findings with, histopathology of MR-guided samples by radiologist.	NA
Niaf et al. (18)	WMHS + MO	MO	Manual registration
Artan and Yetik (147)	WMHS + MO	MO + ex vivo MRI	Manual registration
Shah et al. (17)	WMHS + MO	Not specified	PSM
Matulewicz et al. (57)	WMHS + MO	MO	Manual registration
Hambrock et al. (13)	WMHS + MO	MO	Manual registration
Tiwari et al. (148)	WMHS + MO	MO	Manual registration
Peng et al. (27)	WMHS	MO	Manual registration
Ginsburg et al. (149)	WMHS + MO	Registration from histologic images	Nonlinear registration
Stember et al. (51)	Needle biopsy	Not specified	NA
Niaf et al. (150)	Prostatectomy + MO	MO	Manual registration
Garcia Molina et al. (16)	Prostatectomy + MO	MO	Manual registration
Litjens et al. (62)	Needle biopsy	Not specified	NA
Kwak et al. (52)	Needle biopsy	Determined by radiologists	NA
Zhao et al. (151)	Biopsy	MO	NA

3D, three-dimensional; CADx, computer-aided diagnosis; MACMI, multi-attribute, higher order mutual information based elastic registration scheme; MANTRA, multi-attribute, non-initializing, texture reconstruction based active shape model (ASM); MO, manual outlined regions of lesions; MR, magnetic resonance; NA, no registration was used; PSM, patient-specific molds; WMHS, whole-mount histologic sections.

correlation between MR images and histopathologic images, the corresponding anatomic landmarks and cancerous regions are manually labeled by an expert. The urethra may serve as a guide for correlating the images. To improve the accuracy and efficiency of the correlation, some automatic methods have been developed (111,124).

There are several challenges in establishing automatic correlation between *in vivo* MR images and histopathologic images. The orientation of the specimen and its sections may be different from that of *in vivo* MRI. There are mismatches between MRI and histopathology, which make it difficult to assess the true accuracy of MRI. Once the anatomic orientation in the body is lost, it may be difficult to section the prostate in the same plane as that of *in vivo* MR images. The specimen can be marked with separate colors on the left, right, and anterior aspects for anatomic orientation (111). Using image processing, CAD, and rapid prototyping technology, a customized mold has been used to process prostatectomy specimens for each patient (124). The customized mold holds the prostate in the same position and the same shape as those of *in vivo* MR images and guides the cutting knife to obtain tissue blocks that correspond to the image slices.

The prostate is an easily deformable organ, hence, the gland deforms during and after prostatectomy. Additionally, prostate MRI is often performed by using an ERC, which further deforms the gland. Specimen formalin fixation and paraffin embedding also induce variable tissue shrinkage. Deformable image registration provides a high degree of flexibility for registration of histologic images with *in vivo/ex vivo* MR images, and can assist in more accurate evaluation of MRI findings. Boundary landmarks and internal landmarks of the same prostate have been used in a deformable registration algorithm. Mazaheri et al. describe a semiautomatic method by using a free-form deformation algorithm based on B-splines (125). This method enabled successful registration of anatomic prostate MR images to pathologic slices. Jacobs et al. (126) proposed a method for the registration and warping of MR images to histologic sections. This method consists of a

modified surface-based registration algorithm followed by an automated warping approach using nonlinear thin plate splines to compensate for the distortions between the datasets.

There are two general approaches to map *ex vivo* histologic PCa extent to preoperative MR images. The first method, perhaps the more intuitive approach, is to reconstruct the 3D histologic volume, and then register the 3D histologic volume with the 3D MR volume (127,128). The second approach is to register each two-dimensional (2D) histology slice to its corresponding 2D MRI slice separately (107,129). In the first approach, one critical prerequisite was the accurate reconstruction of the histologic volume, whereas in the second approach, the prerequisite was to determine the histology-MRI slice correspondence. In some cases, the former prerequisite may not be achievable; hence, the only solution is to take the second approach. There is an increasing interest in the registration of 3D histopathology with prostate MRI. Three-dimensional reconstruction of prostate histology facilitates these registration-based evaluations by reintroducing 3D spatial information lost during histology processing (130,131). Patel et al. (132) presented a scheme for the registration of digitally reconstructed whole-mount histology to preoperative *in vivo* mp-MRI using spatially weighted mutual information. McGrath et al. (133) used reference landmarks that are visible in both data sets to assist 3D histopathology reconstruction and thus can provide important information on the deformation effects of fixation, and hence improved registration accuracy. Histostitcher, a software system designed to create a pseudo whole-mount histology section from a stitching of four individual histology quadrant images, is another alternative for reconstructing pseudo whole-mount prostate images (134).

Registering pathologic information to mp-MRI is a challenging problem in developing a CADx system for mp-MRI (Fig 10). Chappelow et al. (135) described a method based on mutual information that registers T2W, DCE-MRI, and ADC. However, this method is based on 2D histology and requires considerable expertise to determine the

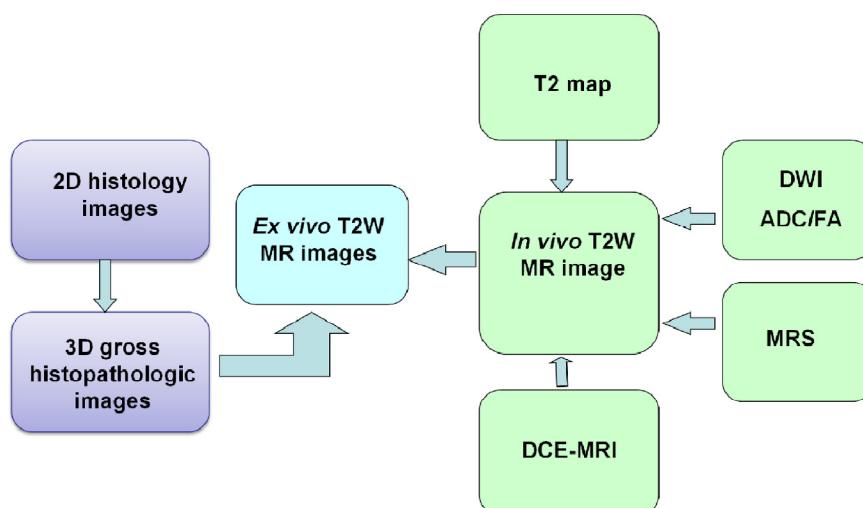


Figure 10. Registration between multi-parametric magnetic resonance imaging (mp-MRI) and histology.

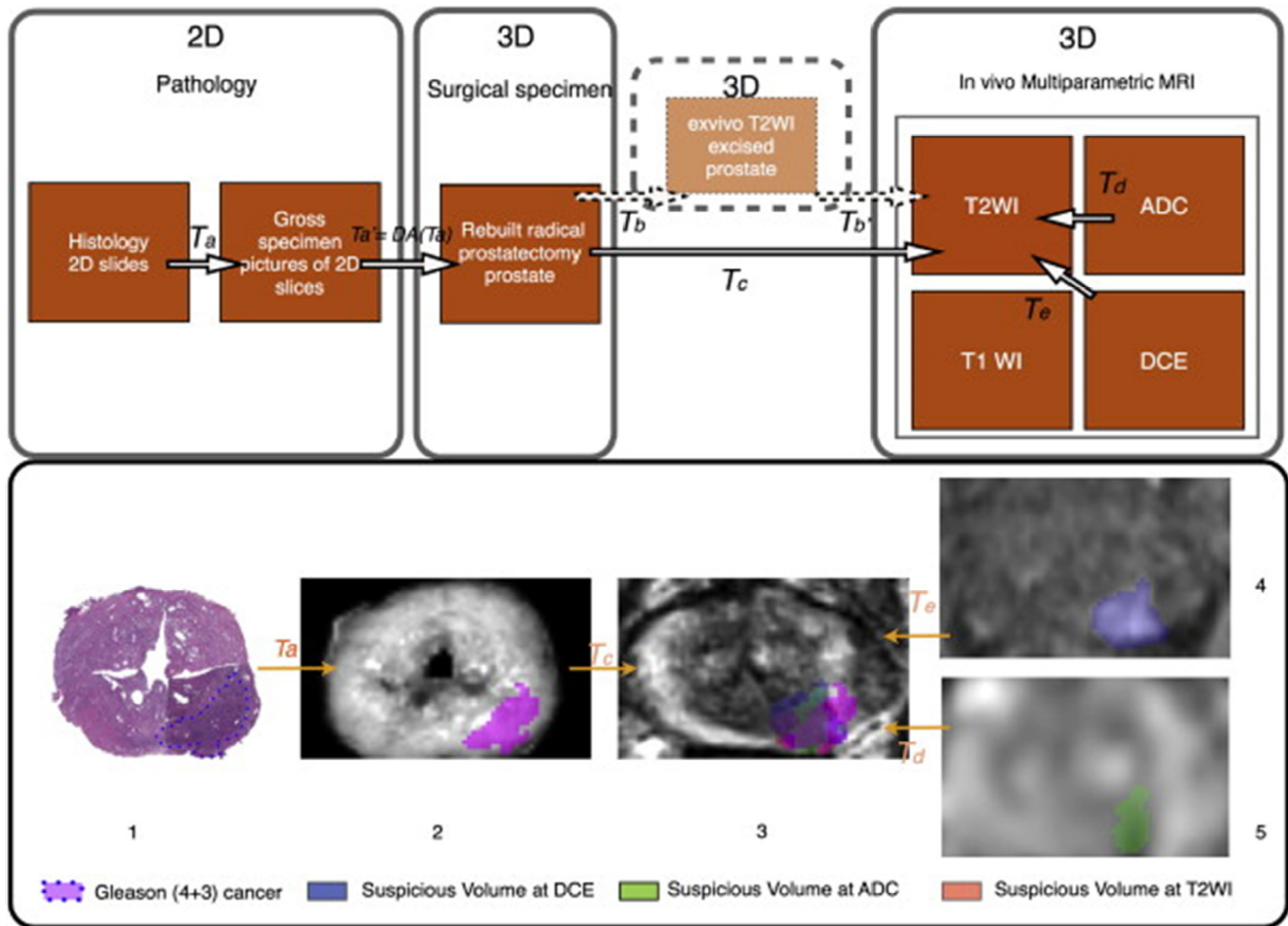


Figure 11. Registration between magnetic resonance imaging (MRI) and histology. **Top:** Workflow for pathology-multiparametric (mp)-MRI registration in a surgical three-dimensional (3D) space. **Bottom:** 3D deformable registration of virtual whole-mount histology (1), fresh specimen (2), T2-weighted MRI (3), perfusion (4), and diffusion (5) sequences (apparent diffusion coefficient [ADC]) applied to prostate cancer (image from Reference (136)).

correspondence between histologic and MR images. Orczyk et al. (136) described a method based on the present registration method and were the first to create a 3D counterpart within the same reference space between histology and both anatomic and functional sequences provided by prostate mp-MRI (Fig 11). The method enables a true, deformable transformation and achieves an accuracy of 1–2 mm. The registration of different MR images is critical considering prostate motion, especially related to rectal peristalsis. Orczyk et al. (136) used rigid registration to correct motion between difference sequences.

Although whole-mount prostate histologic analysis provides accurate label information for training a CADx system, whole-mount histology is expensive and registering whole-mount histologic slices with 3D mp-MRI is a challenging problem. Therefore, histologic interpretations from biopsy specimens are used to determine the ground truth in some studies (14,62,122,137,138). In vivo biopsy can label only the pathology of the core inside the prostate. Radiologists must

manually define lesion boundaries on mp-MRI retrospectively based on the biopsy results.

Meyer et al. (139) reviewed the registration methods of 3D medical images and histopathology of the prostate. They examined the registration process and techniques for registering MRI or positron emission tomography with whole-mounted prostatectomy specimens.

CLINICAL APPLICATIONS

Diagnosis

The functional MRI data, like DCE-MRI and MRS, are more complex and larger in amounts than anatomic MRI. There are clinical needs for the development of fast, cost-effective, supportive techniques, such as computer-aided analysis tools, for easy and more reproducible diagnosis of PCa. Researchers have focused on developing CADx methodology for automated prostate MRS classification and DCE-MRI analysis. Because all functional MRI

techniques have their strengths and shortcomings, single technique cannot adequately detect and characterize PCa. The combination of anatomic (T2W) images and functional techniques has been shown to increase the accuracy of MRI for the diagnosis of PCa. Table 2 compares the performance of the major published prostate CADx systems (13,14,16–18,22,26,27,36,37,39,51,52,54–57,62,122,129,140–151). Chan et al. were one of the first groups who implemented an mp-MRI CADx system for the diagnosis of PCa (122). In their approach, they used line-scan diffusion, T2, and T2W images to identify predefined areas of the PZ of the prostate for the presence of PCa. Viswanath et al. (129) present an mp-MRI CADx system for PCa detection by integrating functional and structural information obtained via DCE and T2W-MRI. Liu et al. (141) present fuzzy Markov random field models for PCa detection of multispectral MR prostate images. Tiwari et al. (55) investigated the use of MRS in combination with T2W-MRI to identify the voxels that are affected by PCa. They also introduced the use of wavelet embedding to map MRS and T2W texture features into a common space. In a study by Peng et al. (27), the combination of 10th percentile ADC, average ADC, and T2W skewness with CADx yielded an AUC value of 0.95 in differentiating PCa from normal tissue. The combination achieved higher accuracy than any MR parameter alone. In a more recent study by Litjens et al. (62), they developed a fully automated CAD system that consists of two stages. The first (detection) stage consists of segmentation of the prostate on the transversal T2W-MRI, extraction of voxel features from the image volumes, classification of the voxels, and candidate selection. The second (diagnosis) stage consists of candidate segmentation, candidate feature extraction, and candidate classification. The system was evaluated on a large consecutive cohort of 347 patients and yielded an AUC value of 0.889.

Aggressiveness

Treatment choice for PCa is based on initial PSA level, clinical stage of disease, and Gleason score, together with baseline urinary function, comorbidities, and patient age (152,153). Therefore, there is an urgent clinical need to detect high-grade cancers and to differentiate them from indolent, slow-growing tumors. The Gleason system, using a rating system to determine the grade of PCa, remains one of the widely used prognostic factors in PCa. The higher grade tumors have a tendency to grow quickly and to spread faster than lower grade tumors.

DWI, DCE-MRI, and MRS are noninvasive assessment methods of PCa aggressiveness. The Gleason grading system is a fundamental indicator of the aggressive nature of PCa. Studies found that ADC image features correlate with Gleason scores (27,28,46,154–156). A study by Yamamura et al. found a highly significant negative correlation between ADC value and the Gleason score, whereas MRS did not show a significant correlation (157). Recently, Zhang et al. found that TRUS-guided, MRI-directed biopsies improved the predic-

tion of PCa aggressiveness in comparison to 12-core TRUS-guided biopsies. DWI-directed biopsies had a superior performance when compared to MRS-directed biopsies in the PZ (6). Diffusion of water molecules in tumor tissue was thought to reflect tissue architecture such as cell density and nucleus-to-cytoplasm ratio, and reductions in ADC values in tumor tissue in fact correlates well with increases in cellular density (158–160). For these reasons, ADC value has received more attention as a predictor of Gleason score in PCa.

DCE-MRI is based on the permeability of blood vessels and extravasation of contrast agent into the surrounding tissue. Investigators have observed that quantitative parameters (K^{trans} and K^{ep}) and semiquantitative parameters (wash-in and washout) derived from DCE-MRI have the potential to assess the aggressiveness of PCa. Oto et al. found a moderate correlation between k^{ep} and microvessel density of PCa (154). Peng et al. found that K^{trans} moderately correlate with Gleason scores (27).

In vivo MRS imaging has revealed a trend toward an increased (choline + creatine)/citrate ratio with increased Gleason score (161,162). This relationship has also been demonstrated by ex vivo high resolution magic angle spinning (HR-MAS) MRS (163). However, other in vivo MRS imaging studies have found no correlation between metabolite ratios and aggressiveness (164,165).

On T2W-MRI, changes in signal intensity for PCa detection have been associated with its aggressiveness (166). In a large retrospective study with 220 patients (166), T2W-MRI and MRS imaging scores based on a three-point scale for clinical PCa aggressiveness were significantly correlated to biologic markers such as androgen receptor levels, which were associated with PCa progression. In that study, the combination of biomarkers with T2W-MRI and MRS imaging results can discriminate clinically unimportant PCa. If mp-MRI can potentially aid in identifying low-grade disease in vivo, this might allow PCa patients to opt for active surveillance rather than immediately opting for aggressive therapy. Lee et al. demonstrated that the simple measurement of the diameter of suspicious tumor lesions on DWI could improve the prediction of insignificant PCa in candidates for active surveillance therapy (167).

Although these MRI metrics are related to Gleason score, the power and threshold value of each metric are different and how to combine these anatomic and functional MRI information is still a problem. Developing a computerized decision support system may help in noninvasive assessment of PCa aggressiveness. Recently, a system called Semi Supervised Multi Kernel Graph Embedding was developed to quantitatively combine T2WI and MRS data to distinguishing benign from cancerous, and high- from low-Gleason grade PCa regions in vivo (148).

Biopsy Guidance

TRUS-guided sextant or systematic prostate biopsy is the clinical standard for definitive diagnosis of PCa. The Gleason score derived from biopsy specimens is important for appropriate

TABLE 2. Summary of Representative Studies in the Literature

Reference	Modality	Validation	Region	Classifier	Data Size	Performance
Chan et al. (122)	T2WI, ADC, T2	Biopsy	PZ	SVM, FLD	15	FLD, AUC = 0.839; SVM, AUC = 0.761
Puech et al. (39)	DCE	Prostatectomy	PZ and TZ	Software titled "ProCAD"	100	PZ, Se/Sp = 100/49%; TZ, Se/Sp = 100/40%
Tiwari et al. (54)	MRS	Biopsy	WP	Spectral clustering	14	Se = 77.8%, FP = 28.92%, and FN = 20.88%
Vos et al. (36)	DCE	WMHS	PZ	SVM	34	AUC = 0.83
Viswanath et al. (140)	DCE	WMHS	WP	LLE and consensus clustering	6	Se = 60.72%, Sp = 83.24%
Viswanath et al. (129)	T2WI, DCE	WMHS	WP	Random forest	6	AUC = 0.815
Vos et al. (37)	DCE	WMHS	PZ	SVM	38	AUC = 0.80
Liu et al. (141)	T2W, T2, ADC, DCE	WMHS	PZ	Fuzzy MRF model	11	Se = 89.58%, Sp = 87.50%
Tiwari et al. (55)	MRS	Prostatectomy	WP	NLDR	18	Se = 89.33%, Sp = 79.79%
Artan et al. (142)	T2, ADC, DCE	Biopsy	PZ	Cost-sensitive CRF	21	AUC = 0.79
Vos et al. (143)	T2WI, DCE	WMHS	PZ	SVM	29	AUC = 0.89
Viswanath et al. (144)	T2W, DWI, DCE	WMHS	WP	EMPrAvISE	12	AUC = 0.77
Lopes et al. (145)	T2WI	WMHS	WP	SVM, AdaBoost	17	SVM, Se/Sp = 83/91%; AdaBoost, Se/Sp = 85/93%
Liu and Yetik (26)	T2W, DWI, DCE	WMHS	WP	SVM	20	AUC = 0.89
Sung et al. (146)	DCE	Prostatectomy	PZ and TZ	SVM	42	PZ, Se/Sp = 89/89%; TZ, Se/Sp = 91/64%
Tiwari et al. (56)	T2WI, MRS	WMHS	WP	Random forest	36	AUC = 0.89
Viswanath et al. (22)	T2WI	WMHS	PZ and CG	QDA	22	CG, AUC = 0.86; PZ, AUC = 0.73
Vos et al. (14)	T1, T2, ADC, DCE	Biopsy	WP	LDA	200	Se = 0.74, at an FP level of 5 per patient
Niaf et al. (18)	T2W, DWI, DCE	WMHS	PZ	SVM	30	AUC = 0.89
Artan and Yetik (147)	T2, ADC, T1-PC	WMHS	WP	SVM	15	Se = 76%, Sp = 86%
Shah et al. (17)	T2WI, ADC, DCE	WMHS	PZ	SVM	31	f-measure = 89%
Matulewicz et al. (57)	MRS	WMHS	WP	ANN	18	AUC = 0.968
Hambrock et al. (13)	T2WI, DWI, DCE	Prostatectomy	PZ and TZ	In-house-developed CAD system	34	Experienced observers, AUC = 0.91
Tiwari et al. (148)	T2WI, MRS	WMHS	WP	SeSMiK-GE	29	AUC = 0.89
Peng et al. (27)	T2WI, ADC, DCE	Prostatectomy	WP	LDA	48	AUC = 0.95
Ginsburg et al. (149)	T2WI, DWI, DCE	WMHS	PZ and CG	PCA-VIP	108	CG, AUC = 0.85; PZ, AUC = 0.79
Stember et al. (51)	T2WI, ADC	Biopsy	TZ	Naive Bayes classifier	18	Predicted TZ tumor in all test patients
Niaf et al. (150)	T2WI, DWI, DCE	Prostatectomy	WP	P-SVM	48	AUC = 0.889
Garcia Molina et al. (16)	T2WI, ADC, DCE	Prostatectomy	PZ	Incremental learning ensemble SVM	12	Se = 84.4%, Sp = 78.0%
Litjens et al. (62)	T2WI, DWI, DCE, PDWI	Biopsy	WP	Random forest	347	AUC = 0.889
Kwak et al. (52)	T2WI, DWI	Biopsy	PZ and TZ	SVM	244	AUC of 0.89
Zhao et al. (151)	T2WI	Biopsy/follow-up	PZ and CG	ANN	71	CG, AUC = 0.821; PZ, AUC = 0.849

ADC, apparent diffusion coefficient; ANN, artificial neural network; AUC, area under a receiver operating characteristic curve; CAD, computer-aided detection; CG, central gland; CRF, conditional random fields; DCE, dynamic contrast-enhanced; EMPrAvISE, Enhanced Multi-Protocol Analysis via Intelligent Supervised Embedding; FLD, Fisher linear discriminant; FN, false negative; FP, false positive; LDA, linear discriminant analysis; LLE, locally linear embedding; MRS, magnetic resonance spectroscopy; NLDR, nonlinear dimensionality reduction; PCA, principal component analysis; PCA-VIP, variable importance on projection measure for PCA; P-SVM, probabilistic SVM; PZ, peripheral zone; QDA, quadratic discriminant analysis; Se, sensitivity; SeSMiK-GE, Semi Supervised Multi Kernel Graph Embedding; Sp, specificity; SVM, support vector machine; T1-PC, principal component of T1-weighted dynamic series; T2WI, T2-weighted imaging; TZ, transition zone; WMHS, whole-mount histologic sections; WP, whole prostate.

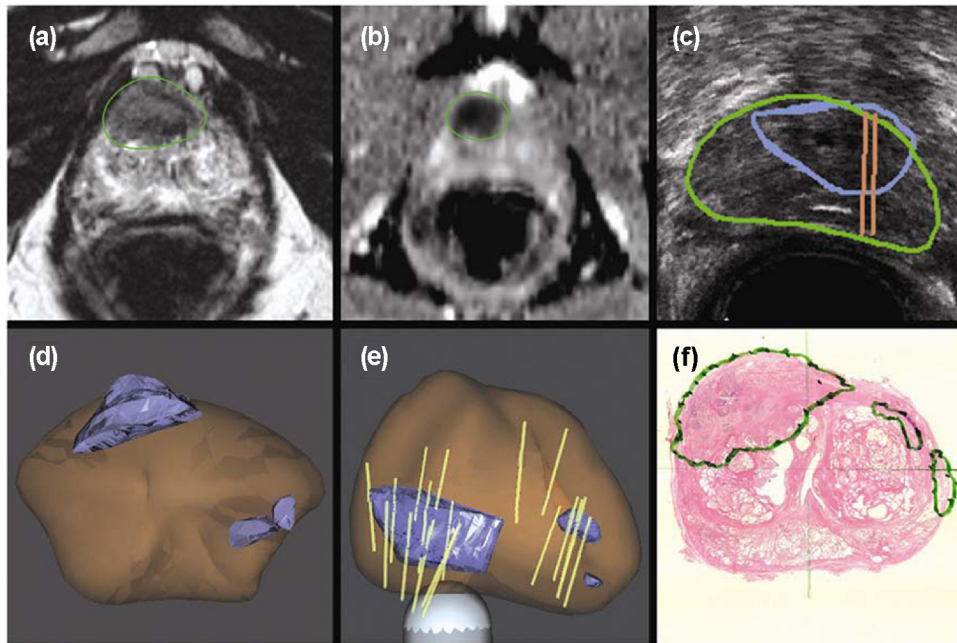


Figure 12. Magnetic resonance imaging (MRI) and ultrasound fusion for targeted biopsy of the prostate. (a, b) Anterior lesion of the high suspicious lesion identified on multiparametric (mp)-MRI. (c) Real-time ultrasound targeting the corresponding lesion. (d, e) Three-dimensional (3D) models demonstrate the target (blue), prostate (brown), and biopsy cores (tan cylinders). (f) Radical prostatectomy pathology confirmed a 2.3 cm Gleason 8 (4 + 4) cancer centered in the right anterior prostate (images from Reference (200)). (Color version of figure is available online.)

treatment selection. However, PCa is often heterogeneous and multicentric (168). In addition, the biopsy, which samples a small portion of the prostate, might not represent the whole gland efficiently. Traditionally, it is believed that Gleason score in systematic random TRUS-guided biopsy tends to downgrade the surgical specimen, because a less-differentiated pattern may not have been sampled in the biopsy (169,170). Systematic random TRUS-guided biopsies often require repeated biopsy procedures, which are associated with discomfort and potential morbidity (171). To reduce the overtreatment and the number of biopsies, lesions must be accurately detected, characterized, and targeted during biopsy. More effective imaging-guided targeted biopsy techniques are under investigation to improve the detection rate of prostate biopsies.

Optimization of prostate biopsy requires addressing the shortcomings of standard systematic TRUS-guided biopsy, including false-negative rates, incorrect risk stratification, detection of clinically insignificant disease, and the need for repeat biopsy. MRI is an evolving noninvasive imaging modality that increases the accurate localization of PCa at the time of biopsy, and thereby enhances clinical risk assessment and improves the ability to appropriately counsel patients regarding therapy.

Use of mp-MRI for targeted prostate biopsies has the potential to reduce the sampling error associated with conventional biopsy by providing better disease localization and sampling, and also has a potential role in avoiding biopsy and reducing over detection/overtreatment. MRI-compatible biopsy systems were developed for this purpose (172). More accurate risk stratification through improved cancer sampling may impact

therapeutic decision making. Optimal clinical application of MRI-targeted biopsy remains under investigation.

There are three different manners in which an MRI-detected lesion can be targeted for biopsy: (1) direct targeting within the magnet using MR-compatible devices, also called in-bore MRI-guided biopsy; (2) use of fusion software to allow an MRI-defined lesion to be identified on ultrasound during a TRUS-guided biopsy procedure (Fig 12); or (3) cognitive targeting, in which the physician reviews the MRI data before the procedure and attempts to target the suspected area during the TRUS-guided biopsy using anatomic landmarks as reference (173). An MRI-guided robotic prostate biopsy system, named the access to prostate tissue under MRI (APT-MRI) robotic biopsy system, has been reported with an accuracy within 2 mm (174). A real-time phase-only cross correlation algorithm-based sequence has been used in transrectal 3 T in-bore MR-guided prostate biopsies (175). Fusion of pre-biopsy MR images onto interventional TRUS images might increase the overall biopsy accuracy (176,177). A novel method to identify the 2D axial MR slice from a pre-acquired MR prostate volume that closely corresponds to the 2D axial TRUS slice obtained during prostate biopsy has been reported by Mitra et al. (178).

Treatment Planning and Therapeutic Response Assessment

MRI-based techniques are used for computer-aided treatment procedures such as treatment planning of radiotherapy, MRI-

guided radioactive seeds placement in prostate brachytherapy, and MRI-guided local ablation procedures (179–190).

The excellent soft-tissue contrast of MRI means that the technique is having an increasing role in contouring the gross tumor volume and organs at risk in radiation therapy treatment planning systems. MRI-planning scans from diagnostic MRI scanners are currently incorporated into the planning process by being registered to CT data. The soft-tissue data from the MRI provide target outline guidance and the CT provides a solid geometric and electron density map for accurate dose calculation on the TPS computer (191).

A number of minimally invasive, focal, organ-preserving methods have been used in recent years as further alternatives to the radical treatment of PCa (170). The focal therapy methods used to date for the prostate include cryotherapy, high-intensity focused ultrasound, laser-induced thermal ablation, and radioactive seed placement. Mp-MRI makes it possible to determine the exact location of tumor foci that are generally accessible for ablation or radioactive seed placement. Moreover, mp-MRI can also monitor treatment during and after minimally invasive therapy. A CADx system for the prostate may have potential value in helping clinicians to target tumor foci during treatment.

Mp-MRI can also be used as an imaging biomarker for monitoring therapeutic response, including radiotherapy of localized PCa (191) and systemic therapy for metastatic disease. Successful treatment response to therapy is usually depicted by reductions in signal intensity accompanied by ADC increases (192–194). There are clinical needs to develop mp-MRI-based CADx systems for monitoring therapeutic response of the prostate in the future.

DISCUSSION AND FUTURE DIRECTIONS

Unlike breast and lung cancer, PCa CADx systems for MR images have not been widely used in daily clinical work for detection or diagnosis. The majority of the prostate CADx systems reported the AUC in the range from 0.80 to 0.89 (179), whereas one reported AUCs of 0.96 (46), which represented a high performance. However, most systems generated lesion candidates based on manually selected ROIs, which may be data set dependent, and employed a relatively small data set. Validation on a large-scale data set with several hundred patients is required. A prostate CADx system should be tested in multicenter trials to make the systems widely usable in clinical work.

One challenge of prostate CAD is related to mp-MRI protocols. Both 3 T protocols and ERCs have the advantage of increasing the signal-to-noise ratio. At 3 T without the use of an ERC, image quality can be comparable to that obtained at 1.5 T with an ERC (195). Turkbey et al. found that dual-coil prostate MRI detected more cancer foci than non-ERC MRI at 3 T on T2W and DWI (196). At 3 T MRI, DWI images and ADC maps using $b = 1500 \text{ s/mm}^2$ should be considered more effective than those at $b = 2000 \text{ s/mm}^2$ or $b = 1000 \text{ s/mm}^2$ for PCa detection (50). Most members

of the PI-RADS steering committee recommend 3 T for prostate MRI. There is no consensus among experts concerning the potential benefits of the use of ERCs (12). The impact of the mp-MRI protocol on CADx systems should be considered and researched in the future. The combination of T2W, DWI, and DCE-MRI is the most commonly used set of parameters for the detection or diagnosis of PCa. MRS with other parameters is also used in some research. The introduction of new imaging modalities or new modality combinations for mp-MRI may lead to better CADx systems. Combining CAD prediction and PI-RADS into a combination score has the potential to improve diagnostic accuracy (197). The MR PI-RADS system may provide a platform for CAD system development in the future.

The diagnostic value of these parameters for discrimination between benign tissue and malignant tissue depends on the lesion's location. The parameter values of PCa are in the range of those of nonmalignant diseases or conditions such as prostatitis, fibromuscular benign prostatic hyperplasia, post-biopsy hemorrhagic change, making for poor diagnostic value, especially in the TZ. TZ and PZ cancer possess distinct quantitative imaging features on MRI. Computer-extracted parameters may be useful for cancer detection in the PZ, but are not suited in the TZ. In recent years, research focus has shifted from PZ PCa to whole PCa. There are more challenges in developing a CADx system for both PZ and TZ lesions than for PZ lesions only. Applications of anatomic segmentation from MRI as an additional input to artificial neural network improve the accuracy of detecting cancerous voxels from MRSI (198). A CAD system, using two MRI sequences, such as T2-MRI and high b -value ($b = 2000 \text{ s/mm}^2$) DWI, and texture features based on local binary patterns, is able to detect the discriminative texture features for cancer detection and localization, and the performance of the CADx system was not dependent on the specific regions of the prostate (52). Future direction should also include whether zonal segmentation of the prostate is necessary when some new imaging sequences are being used.

Ex vivo whole-mount prostate histologic analysis provides more accurate label information for training a CADx system. However, whole-mount histology is expensive, and registering whole-mount histologic slices with 3D mp-MRI is a challenging problem. This is especially true during the preparation of the prostate histologic data for training a CADx system. Pathologists must collect a large amount of training data from many patients, apply reliable biomarkers for each patient, prepare blocks, scan a large number of histologic slices, and manually define lesion boundaries on histologic slices. However, these are laborious and time-consuming procedures. Therefore, the histologic image preparation procedures need to be performed by some automatic methods to improve efficacy. A software system has been designed to create a pseudo whole-mount histology section (134). A computer-aided system to automatically grade pathologic images according to the Gleason grading system has also been investigated (199). A scheme, including automatic diagnosis from histologic images,

3D histologic reconstruction, and registration, should be developed for ground truth definition in the future.

Image quantification methods, such as accurate image registration for motion correction, compartment modeling for functional parameters estimation, feature extraction in high-dimensional data, automatic image classification for differentiating cancer from normal tissue, and correlation analyses among radiological data and genomic information, will play key roles in the future development of intelligent CAD systems.

Radiomics, as a high-dimensional extraction of large amounts of image features with high throughput from radiographic images, can provide valuable diagnostic, prognostic, or predictive information. Cameron et al. had developed a quantitative radiomics feature model for performance of PCa detection using mp-MRI (115). Khalvati et al. (118) present new texture feature models for radiomics-driven detection of PCa using mp-MRI data. Radiomics are emerging as a useful tool for PCa detection. Further work is needed to build radiomics-based CAD systems for PCa diagnosis, treatment planning, treatment prediction, and treatment response evaluation.

The Gleason grade of PCa is the most widely used prognostic factor for PCa. MR metrics on T2W, DWI, DCE-MRI, and MRS imaging relate to microenvironment and microstructure. Therefore, these MR metrics can predict the Gleason grade of the cancer. Building a CAD system based on mp-MRI and Gleason score is feasible. It can play a significant role in predicting prognosis, guiding biopsy, identifying suitable patients under active surveillance, and making a decision of appropriate treatment. CAD systems for prediction of Gleason score should be developed in the future.

As the anatomic information is important when analyzing functional data, T2W images are frequently used in mp-MRI CADx systems. T2W plus DWI and DCE-MRI are commonly used as the combinations. Chan et al. constructed a summary statistical map of the PZ based on the utility of multichannel statistical classifiers by combining textural and anatomic features in PCa areas from T2W, DWI, proton density maps, and T2 maps (122). Langer et al. included DCE-MRI and PK parameter maps as extra features to a CADx system for the detection of PCa at the PZ (111). They evaluated their system in predefined ROIs, but on a per voxel basis. Vos et al. implemented a two-stage CADx system for PCa using an initial blob detection approach combined with a candidate segmentation and classification using statistical region features (14). Litjens et al. recently investigated a fully automated CAD system including a novel combination of segmentation, voxel classification, candidate extraction, and classification (62).

Promising preliminary results have been obtained with CADx systems that combine the analysis of statistical, structural, and functional MRI features and the use of an adapted classification scheme. Likelihood maps have been obtained by combining information from mp-MRI using mathematical descriptors. These studies showed that the discrimination between

benign and malignant tissues is feasible with good performances (62,111).

CONCLUSION

We comprehensively reviewed mp-MRI-based, computer-aided technology for PCa detection. Prostate CADx systems are a complicated composition of preprocessing, segmentation, registration, feature extraction, and classification modules. There are some challenges in accurate registration of MRI and histopathology, which is important for ground truth definition. Clinical applications of computer-aided systems include localization, diagnosis, staging, aggressiveness assessment, guiding biopsy, treatment planning, and therapeutic response assessment. Although the performance of some CADx systems is good, there is no such a system that has been widely used in clinic. It is likely that more improvements in quantitative image analysis and computer-aided methods would need to be made to meet the clinical needs in near future work.

ACKNOWLEDGMENTS

This work was partially supported by NIH grants R01CA156775, R21CA176684, and P50CA128301. Z. Zhang was supported by the National Natural Science Foundation of China (81372274). The work was also partially supported by a Georgia Research Alliance Distinguished Scientists Award.

REFERENCES

1. Siegel RL, Miller KD, Jemal A. Cancer statistics, 2015. *CA Cancer J Clin* 2015; 65:5–29.
2. Lee JJ, Thomas IC, Nolley R, et al. Biologic differences between peripheral and transition zone prostate cancer. *Prostate* 2015; 75:183–190.
3. Siddiqui MM, Rais-Bahrami S, Turkbey B, et al. Comparison of MR/ultrasound fusion-guided biopsy with ultrasound-guided biopsy for the diagnosis of prostate cancer. *JAMA* 2015; 313:390–397.
4. Pokorny MR, de Rooij M, Duncan E, et al. Prospective study of diagnostic accuracy comparing prostate cancer detection by transrectal ultrasound-guided biopsy versus magnetic resonance (MR) imaging with subsequent MR-guided biopsy in men without previous prostate biopsies. *Eur Urol* 2014; 66:22–29.
5. Schoots IG, Roobol MJ, Nieboer D, et al. Magnetic resonance imaging-targeted biopsy may enhance the diagnostic accuracy of significant prostate cancer detection compared to standard transrectal ultrasound-guided biopsy: a systematic review and meta-analysis. *Eur Urol* 2015; 68:438–450.
6. Zhang J, Xiu J, Dong Y, et al. Magnetic resonance imaging-directed biopsy improves the prediction of prostate cancer aggressiveness compared with a 12-core transrectal ultrasound-guided prostate biopsy. *Mol Med Rep* 2014; 9:1989–1997.
7. Brown AM, Elbuluk O, Merten F, et al. Recent advances in image-guided targeted prostate biopsy. *Abdom Imaging* 2015; 40:1788–1799.
8. Puech P, Rouviere O, Renard-Penna R, et al. Prostate cancer diagnosis: multiparametric MR-targeted biopsy with cognitive and transrectal US-MR fusion guidance versus systematic biopsy—prospective multicenter study. *Radiology* 2013; 268:461–469.
9. Lawrence EM, Tang SY, Barrett T, et al. Prostate cancer: performance characteristics of combined T2W and DW-MRI scoring in the setting of template transperineal re-biopsy using MR-TRUS fusion. *Eur Radiol* 2014; 24:1497–1505.

10. Barentsz JO, Richenberg J, Clements R, et al. ESUR prostate MR guidelines. *Eur Radiol* 2012; 2012:746–757.
11. Dickinson L, Ahmed HU, Allen C, et al. Magnetic resonance imaging for the detection, localisation, and characterisation of prostate cancer: recommendations from a European consensus meeting. *Eur Urol* 2011; 59:477–494.
12. Weinreb JC, Barentsz JO, Choyke PL, et al. PI-RADS Prostate Imaging-Reporting and Data System: 2015, version 2. *Eur Urol* 2016; 69:16–40.
13. Hambroek T, Vos PC, Hulsbergen-van de Kaa CA, et al. Prostate cancer: computer-aided diagnosis with multiparametric 3-T MR imaging—effect on observer performance. *Radiology* 2013; 266:521–530.
14. Vos PC, Barentsz JO, Karssemeijer N, et al. Automatic computer-aided detection of prostate cancer based on multiparametric magnetic resonance image analysis. *Phys Med Biol* 2012; 57:1527–1542.
15. Niaf E, Lartzien C, Bratan F, et al. Prostate focal peripheral zone lesions: characterization at multiparametric MR imaging—influence of a computer-aided diagnosis system. *Radiology* 2014; 271:761–769.
16. Garcia Molina JF, Zheng L, Serdemir M, et al. Incremental learning with SVM for multimodal classification of prostatic adenocarcinoma. *PLoS ONE* 2014; 9:e93600.
17. Shah V, Turkbey B, Mani H, et al. Decision support system for localizing prostate cancer based on multiparametric magnetic resonance imaging. *Med Phys* 2012; 39:4093–4103.
18. Niaf E, Rouviere O, Mege-Lechevallier F, et al. Computer-aided diagnosis of prostate cancer in the peripheral zone using multiparametric MRI. *Phys Med Biol* 2012; 57:3833–3851.
19. Akin O, Sala E, Moskowitz CS, et al. Transition zone prostate cancers: features, detection, localization, and staging at endorectal MR imaging. *Radiology* 2006; 239:784–792.
20. Li H, Sugimura K, Kaji Y, et al. Conventional MRI capabilities in the diagnosis of prostate cancer in the transition zone. *AJR Am J Roentgenol* 2006; 186:729–742.
21. Cornud F, Rouanne M, Beuvon F, et al. Endorectal 3D T2-weighted 1 mm-slice thickness MRI for prostate cancer staging at 1.5Tesla: should we reconsider the indirect signs of extracapsular extension according to the D'Amico tumor risk criteria? *Eur J Radiol* 2012; 81:e591–e597.
22. Viswanath SE, Bloch NB, Chappelou JC, et al. Central gland and peripheral zone prostate tumors have significantly different quantitative imaging signatures on 3 Tesla endorectal, in vivo T2-weighted MR imagery. *J Magn Reson Imaging* 2012; 36:213–224.
23. Hoeks CM, Hambroek T, Yakar D, et al. Transition zone prostate cancer: detection and localization with 3-T multiparametric MR imaging. *Radiology* 2013; 266:207–217.
24. Liu W, Turkbey B, Senegas J, et al. Accelerated T2 mapping for characterization of prostate cancer. *Magn Reson Med* 2011; 65:1400–1406.
25. Yamauchi FI, Penzkofer T, Fedorov A, et al. Prostate cancer discrimination in the peripheral zone with a reduced field-of-view T2-mapping MRI sequence. *Magn Reson Imaging* 2015; 33:525–530.
26. Liu X, Yetik IS. Automated prostate cancer localization without the need for peripheral zone extraction using multiparametric MRI. *Med Phys* 2011; 38:2986–2994.
27. Peng Y, Jiang Y, Yang C, et al. Quantitative analysis of multiparametric prostate MR images: differentiation between prostate cancer and normal tissue and correlation with Gleason score—a computer-aided diagnosis development study. *Radiology* 2013; 267:787–796.
28. Nowak J, Malzahn U, Baur AD, et al. The value of ADC, T2 signal intensity, and a combination of both parameters to assess Gleason score and primary Gleason grades in patients with known prostate cancer. *Acta Radiol* 2016; 57:107–114.
29. Hoang Dinh A, Souchon R, Melodelima C, et al. Characterization of prostate cancer using T2 mapping at 3T: a multi-scanner study. *Diagn Interv Imaging* 2015; 96:365–372.
30. Durmus T, Baur A, Hamm B. Multiparametric magnetic resonance imaging in the detection of prostate cancer. *Aktuelle Urol* 2014; 45:119–126.
31. Ewing JR, Bagher-Ebadian H. Model selection in measures of vascular parameters using dynamic contrast-enhanced MRI: experimental and clinical applications. *NMR Biomed* 2013; 26:1028–1041.
32. Tofts PS, Brix G, Buckley DL, et al. Estimating kinetic parameters from dynamic contrast-enhanced T1-weighted MRI of a diffusable tracer: standardized quantities and symbols. *J Magn Reson Imaging* 1999; 10:223–232.
33. Fedorov A, Fluckiger J, Ayers GD, et al. A comparison of two methods for estimating DCE-MRI parameters via individual and cohort based AIFs in prostate cancer: a step towards practical implementation. *Magn Reson Imaging* 2014; 32:321–329.
34. Gliozzi AS, Mazzetti S, Delsanto PP, et al. Phenomenological universalities: a novel tool for the analysis of dynamic contrast enhancement in magnetic resonance imaging. *Phys Med Biol* 2011; 56:573–586.
35. Mazzetti S, Gliozzi AS, Bracco C, et al. Comparison between PUN and Tofts models in the quantification of dynamic contrast-enhanced MR imaging. *Phys Med Biol* 2012; 57:8443–8453.
36. Vos PC, Hambroek T, Hulsbergen-van de Kaa CA, et al. Computerized analysis of prostate lesions in the peripheral zone using dynamic contrast enhanced MRI. *Med Phys* 2008; 35:888–899.
37. Vos PC, Hambroek T, Barentsz JO, et al. Automated calibration for computerized analysis of prostate lesions using pharmacokinetic magnetic resonance images. *Med Image Comput Comput Assist Interv* 2009; 12:836–843.
38. Puech P, Betrouni N, Makni N, et al. Computer-assisted diagnosis of prostate cancer using DCE-MRI data: design, implementation and preliminary results. *Int J Comput Assist Radiol Surg* 2009; 4:1–10.
39. Puech P, Betrouni N, Viard R, et al. Prostate cancer computer-assisted diagnosis software using dynamic contrast-enhanced MRI. *Conf Proc IEEE Eng Med Biol Soc* 2007; 2007:5567–5570.
40. Padhani AR, Gapinski CJ, Mavvicar DA, et al. Dynamic contrast enhanced MRI of prostate cancer: correlation with morphology and tumour stage, histological grade and PSA. *Clin Radiol* 2000; 55:99–109.
41. Dikaïos N, Alkalbani J, Abd-Alazeez M, et al. Zone-specific logistic regression models improve classification of prostate cancer on multiparametric MRI. *Eur Radiol* 2015; 25:2727–2737.
42. Yacoub JH, Oto A, Miller FH. MR imaging of the prostate. *Radiol Clin North Am* 2014; 52:811–837.
43. Toivonen J, Merisaari H, Pesola M, et al. Mathematical models for diffusion-weighted imaging of prostate cancer using b values up to 2000 s/mm²: correlation with Gleason score and repeatability of region of interest analysis. *Magn Reson Med* 2015; 74:1116–1124.
44. Boesen L, Chabanova E, Logager V, et al. Apparent diffusion coefficient ratio correlates significantly with prostate cancer Gleason score at final pathology. *J Magn Reson Imaging* 2015; 42:446–453.
45. Mazaheri Y, Shukla-Dave A, Hricak H, et al. Prostate cancer: identification with combined diffusion-weighted MR imaging and 3D 1H MR spectroscopic imaging—correlation with pathologic findings. *Radiology* 2008; 246:480–488.
46. Peng Y, Jiang Y, Antic T, et al. Validation of quantitative analysis of multiparametric prostate MR images for prostate cancer detection and aggressiveness assessment: a cross-imager study. *Radiology* 2014; 271:461–471.
47. Kitajima K, Takahashi S, Ueno Y, et al. Clinical utility of apparent diffusion coefficient values obtained using high b-value when diagnosing prostate cancer using 3 tesla MRI: comparison between ultra-high b-value (2000 s/mm²) and standard high b-value (1000 s/mm²). *J Magn Reson Imaging* 2012; 36:198–205.
48. Kim CK, Park BK, Kim B. High-b-value diffusion-weighted imaging at 3 T to detect prostate cancer: comparisons between b values of 1000 and 2000 s/mm². *AJR Am J Roentgenol* 2010; 194:W33–W37.
49. Wetter A, Nensa F, Lipponer C, et al. High and ultra-high b-value diffusion-weighted imaging in prostate cancer: a quantitative analysis. *Acta Radiol* 2015; 56:1009–1015.
50. Wang X, Qian Y, Liu B, et al. High-b-value diffusion-weighted MRI for the detection of prostate cancer at 3 T. *Clin Radiol* 2014; 69:1165–1170.
51. Stember JN, Deng FM, Taneja SS, et al. Pilot study of a novel tool for input-free automated identification of transition zone prostate tumors using T2- and diffusion-weighted signal and textural features. *J Magn Reson Imaging* 2014; 40:301–305.
52. Kwak JT, Xu S, Wood BJ, et al. Automated prostate cancer detection using T2-weighted and high-b-value diffusion-weighted magnetic resonance imaging. *Med Phys* 2015; 42:2368–2378.
53. Neto JA, Parente DB. Multiparametric magnetic resonance imaging of the prostate. *Magn Reson Imaging Clin N Am* 2013; 21:409–426.
54. Tiwari P, Madabhushi A, Rosen M. A hierarchical unsupervised spectral clustering scheme for detection of prostate cancer from magnetic resonance spectroscopy (MRS). *Med Image Comput Comput Assist Interv* 2007; 10:278–286.

55. Tiwari P, Rosen M, Madabhushi A. A hierarchical spectral clustering and nonlinear dimensionality reduction scheme for detection of prostate cancer from magnetic resonance spectroscopy (MRS). *Med Phys* 2009; 36:3927–3939.
56. Tiwari P, Viswanath S, Kurhanewicz J, et al. Multimodal wavelet embedding representation for data combination (MaWERiC): integrating magnetic resonance imaging and spectroscopy for prostate cancer detection. *NMR Biomed* 2012; 25:607–619.
57. Matulewicz L, Jansen JF, Bokacheva L, et al. Anatomic segmentation improves prostate cancer detection with artificial neural networks analysis of 1H magnetic resonance spectroscopic imaging. *J Magn Reson Imaging* 2014; 40:1414–1421.
58. Panebianco V, Barchetti F, Sciarra A, et al. In vivo 3D neuroanatomical evaluation of periprostatic nerve plexus with 3T-MR diffusion tensor imaging. *Eur J Radiol* 2013; 82:1677–1682.
59. Sinha S, Sinha U. In vivo diffusion tensor imaging of the human prostate. *Magn Reson Med* 2004; 52:530–537.
60. Xu J, Humphrey PA, Kibel AS, et al. Magnetic resonance diffusion characteristics of histologically defined prostate cancer in humans. *Magn Reson Med* 2009; 61:842–850.
61. Takayama Y, Kishimoto R, Hanaoka S, et al. ADC value and diffusion tensor imaging of prostate cancer: changes in carbon-ion radiotherapy. *J Magn Reson Imaging* 2008; 27:1331–1335.
62. Litjens G, Debats O, Barentsz J, et al. Computer-aided detection of prostate cancer in MRI. *IEEE Trans Med Imaging* 2014; 33:1083–1092.
63. Suo S, Chen X, Wu L, et al. Non-Gaussian water diffusion kurtosis imaging of prostate cancer. *Magn Reson Imaging* 2014; 32:421–427.
64. Roethke MC, Kuder TA, Kuru TH, et al. Evaluation of diffusion kurtosis imaging versus standard diffusion imaging for detection and grading of peripheral zone prostate cancer. *Invest Radiol* 2015; 50:483–489.
65. Suga M, Aga T, Minato K. Development of a magnetic resonance elastic microscope system. *Conf Proc IEEE Eng Med Biol Soc* 2004; 2:1025–1027.
66. Venkatesh SK, Yin M, Glockner JF, et al. MR elastography of liver tumors: preliminary results. *AJR Am J Roentgenol* 2008; 190:1534–1540.
67. Hamhaber U, Klatt D, Papazoglou S, et al. In vivo magnetic resonance elastography of human brain at 7 T and 1.5 T. *J Magn Reson Imaging* 2010; 32:577–583.
68. Sinkus R, Tanter M, Xydeas T, et al. Viscoelastic shear properties of in vivo breast lesions measured by MR elastography. *Magn Reson Imaging* 2005; 23:159–165.
69. McKnight AL, Kugel JL, Rossman PJ, et al. MR elastography of breast cancer: preliminary results. *AJR Am J Roentgenol* 2002; 178:1411–1417.
70. Sinkus R, Lorenzen J, Schrader D, et al. High-resolution tensor MR elastography for breast tumour detection. *Phys Med Biol* 2000; 45:1649–1664.
71. Arani A, Da Rosa M, Ramsay E, et al. Incorporating endorectal MR elastography into multi-parametric MRI for prostate cancer imaging: initial feasibility in volunteers. *J Magn Reson Imaging* 2013; 38:1251–1260.
72. Li S, Chen M, Wang W, et al. A feasibility study of MR elastography in the diagnosis of prostate cancer at 3.0 T. *Acta Radiol* 2011; 52:354–358.
73. Arani A, Plewes D, Krieger A, et al. The feasibility of endorectal MR elastography for prostate cancer localization. *Magn Reson Med* 2011; 66:1649–1657.
74. Fennessy FM, Fedorov A, Gupta SN, et al. Practical considerations in T1 mapping of prostate for dynamic contrast enhancement pharmacokinetic analyses. *Magn Reson Imaging* 2012; 30:1224–1233.
75. Fortuin AS, Smeenk RJ, Meijer HJ, et al. Lymphotropic nanoparticle-enhanced MRI in prostate cancer: value and therapeutic potential. *Curr Urol Rep* 2014; 15:389.
76. Thoeny HC, Triantafyllou M, Birkhaeuser FD, et al. Combined ultrasmall superparamagnetic particles of iron oxide-enhanced and diffusion-weighted magnetic resonance imaging reliably detect pelvic lymph node metastases in normal-sized nodes of bladder and prostate cancer patients. *Eur Urol* 2009; 55:761–769.
77. Derhy S, El Mouhadi S, Ruiz A, et al. Non-contrast 3D MR lymphography of retroperitoneal lymphatic aneurysmal dilatation: a continuous spectrum of change from normal variants to cystic lymphangioma. *Insights Imaging* 2013; 4:753–758.
78. Arrive L, Derhy S, El Mouhadi S, et al. Noncontrast magnetic resonance lymphography. *J Reconstr Microsurg* 2016; 32:80–86.
79. Collewet G, Strzelecki M, Mariette F. Influence of MRI acquisition protocols and image intensity normalization methods on texture classification. *Magn Reson Imaging* 2004; 22:81–91.
80. Vovk U, Pernuš F, Likar B. MRI intensity inhomogeneity correction by combining intensity and spatial information. *Phys Med Biol* 2004; 49:4119.
81. Vovk U, Pernuš F, Likar B. A review of methods for correction of intensity inhomogeneity in MRI. *IEEE Trans Med Imaging* 2007; 26:405–421.
82. Sled JG, Zijdenbos AP, Evans AC. A nonparametric method for automatic correction of intensity nonuniformity in MRI data. *IEEE Trans Med Imaging* 1998; 17:87–97.
83. Tustison NJ, Avants BB, Cook PA, et al. N4ITK: improved N3 bias correction. *IEEE Trans Med Imaging* 2010; 29:1310–1320.
84. Qiu W, Yuan J, Ukwatta E, et al. Dual optimization based prostate zonal segmentation in 3D MR images. *Med Image Anal* 2014; 18:660–673.
85. Mahapatra D, Buhmann JM. Prostate MRI segmentation using learned semantic knowledge and graph cuts. *IEEE Trans Biomed Eng* 2014; 61:756–764.
86. Liao S, Gao Y, Oto A, et al. Representation learning: a unified deep learning framework for automatic prostate MR segmentation. *Med Image Comput Assist Interv* 2013; 16:254–261.
87. Toth R, Madabhushi A. Multifeature landmark-free active appearance models: application to prostate MRI segmentation. *IEEE Trans Med Imaging* 2012; 31:1638–1650.
88. Litjens G, Debats O, van de Ven W, et al. A pattern recognition approach to zonal segmentation of the prostate on MRI. *Med Image Comput Assist Interv* 2012; 15:413–420.
89. Qiu W, Yuan J, Ukwatta E, et al. Prostate segmentation: an efficient convex optimization approach with axial symmetry using 3-D TRUS and MR images. *IEEE Trans Med Imaging* 2014; 33:947–960.
90. Yang M, Li X, Turkbey B, et al. Prostate segmentation in MR images using discriminant boundary features. *IEEE Trans Biomed Eng* 2013; 60:479–488.
91. Zwiggelaar R, Zhu Y, Williams S. Semi-automatic segmentation of the prostate. In: *Pattern recognition and image analysis*. Springer, 2003; 1108–1116.
92. Flores-Tapia D, Thomas G, Venugopala N, et al. Semi automatic MRI prostate segmentation based on wavelet multiscale products. In: *Engineering in Medicine and Biology Society, 2008 EMBS 2008 30th Annual International Conference of the IEEE*. IEEE, 2008; 3020–3023.
93. Samiee M, Thomas G, Fazel-Rezai R. Semi-automatic prostate segmentation of MR images based on flow orientation. In: *IEEE International Symposium on Signal Processing and Information Technology, 2006*. IEEE, 2006; 203–207.
94. Cootes TF, Hill A, Taylor CJ, et al. The use of active shape models for locating structures in medical images. In: *Information processing in medical imaging*. Springer, 1993; 33–47.
95. Zhu Y, Williams S, Zwiggelaar R. A hybrid ASM approach for sparse volumetric data segmentation. *Pattern Recognit Image Anal* 2007; 17:252–258.
96. Kass M, Witkin A, Terzopoulos D. Snakes: active contour models. *Int J Comput Vis* 1988; 1:321–331.
97. Chan TF, Vese LA. Active contours without edges. *IEEE Trans Image Process* 2001; 10:266–277.
98. Mumford D, Shah J. Optimal approximations by piecewise smooth functions and associated variational problems. *Commun Pure Appl Math* 1989; 42:577–685.
99. Klein S, van der Heide UA, Lips IM, et al. Automatic segmentation of the prostate in 3D MR images by atlas matching using localized mutual information. *Med Phys* 2008; 35:1407–1417.
100. Boykov Y, Veksler O, Zabih R. Fast approximate energy minimization via graph cuts. *IEEE Trans Pattern Anal Mach Intell* 2001; 23:1222–1239.
101. Boykov YY, Jolly M-P. Interactive graph cuts for optimal boundary & region segmentation of objects in ND images. In: *2001 Proceedings Eighth IEEE International Conference on Computer Vision, 2001 ICCV*. IEEE, 2001; 105–112.
102. Egger J. PCG-cut: graph driven segmentation of the prostate central gland. *PLoS ONE* 2013; 8:e76645.
103. Tian Z, Liu L, Fei B. A supervoxel-based segmentation for prostate MR images. *Proc SPIE* 2015; 9413:941318.

104. Litjens G, Toth R, van de Ven W, et al. Evaluation of prostate segmentation algorithms for MRI: the PROMISE12 challenge. *Med Image Anal* 2014; 18:359–373.
105. Ghose S, Oliver A, Marti R, et al. A survey of prostate segmentation methodologies in ultrasound, magnetic resonance and computed tomography images. *Comput Methods Programs Biomed* 2012; 108:262–287.
106. Oliveira FP, Tavares JMR. Medical image registration: a review. *Comput Methods Biomech Biomed Engin* 2014; 17:73–93.
107. Chappelow J, Madabhushi A, Rosen M, et al. Multimodal image registration of ex vivo 4 Tesla MRI with whole mount histology for prostate cancer detection. *Proc SPIE* 2007; 6512:65121S.
108. Kalavagunta C, Zhou X, Schmechel SC, et al. Registration of in vivo prostate MRI and pseudo-whole mount histology using Local Affine Transformations guided by Internal Structures (LATIS). *J Magn Reson Imaging* 2015; 41:1104–1114.
109. Huisman HJ, Engelbrecht MR, Barentsz JO. Accurate estimation of pharmacokinetic contrast-enhanced dynamic MRI parameters of the prostate. *J Magn Reson Imaging* 2001; 13:607–614.
110. Li Q, Sone S, Doi K. Selective enhancement filters for nodules, vessels, and airway walls in two-and three-dimensional CT scans. *Med Phys* 2003; 30:2040–2051.
111. Langer DL, van der Kwast TH, Evans AJ, et al. Prostate cancer detection with multi-parametric MRI: logistic regression analysis of quantitative T2, diffusion-weighted imaging, and dynamic contrast-enhanced MRI. *J Magn Reson Imaging* 2009; 30:327–334.
112. Murase K. Efficient method for calculating kinetic parameters using T1-weighted dynamic contrast-enhanced magnetic resonance imaging. *Magn Reson Med* 2004; 51:858–862.
113. Lambin P, Rios-Velazquez E, Leijenaar R, et al. Radiomics: extracting more information from medical images using advanced feature analysis. *Eur J Cancer* 2012; 48:441–446.
114. Kumar V, Gu Y, Basu S, et al. Radiomics: the process and the challenges. *Magn Reson Imaging* 2012; 30:1234–1248.
115. Cameron A, Khalvati F, Haider M, et al. MAPS: a quantitative radiomics approach for prostate cancer detection. *IEEE Trans Biomed Eng* 2015; doi:10.1109/TBME.2015.2485779.
116. Wibmer A, Hricak H, Gondo T, et al. Haralick texture analysis of prostate MRI: utility for differentiating non-cancerous prostate from prostate cancer and differentiating prostate cancers with different Gleason scores. *Eur Radiol* 2015; 25:2840–2850.
117. Fehr D, Veeraraghavan H. Automatic classification of prostate cancer Gleason scores from multiparametric magnetic resonance images. *Proc Natl Acad Sci USA* 2015; 112:E6265–E6273.
118. Khalvati F, Wong A, Haider MA. Automated prostate cancer detection via comprehensive multi-parametric magnetic resonance imaging texture feature models. *BMC Med Imaging* 2015; 15:27.
119. Breiman L. Random forests. *Mach Learn* 2001; 45:5–32.
120. Friedman J, Hastie T, Tibshirani R. Additive logistic regression: a statistical view of boosting (With discussion and a rejoinder by the authors). *Ann Stat* 2000; 28:337–407.
121. Baeza-Yates R, Ribeiro-Neto B. Modern information retrieval. New York: ACM Press, 1999.
122. Chan I, Wells W, 3rd, Mulker RV, et al. Detection of prostate cancer by integration of line-scan diffusion, T2-mapping and T2-weighted magnetic resonance imaging; a multichannel statistical classifier. *Med Phys* 2003; 30:2390–2398.
123. Donati OF, Mazaheri Y, Afaq A, et al. Prostate cancer aggressiveness: assessment with whole-lesion histogram analysis of the apparent diffusion coefficient. *Radiology* 2014; 271:143–152.
124. Shah V, Pohida T, Turkbey B, et al. A method for correlating in vivo prostate magnetic resonance imaging and histopathology using individualized magnetic resonance-based molds. *Rev Sci Instrum* 2009; 80:104301.
125. Mazaheri Y, Bokacheva L, Kroon DJ, et al. Semi-automatic deformable registration of prostate MR images to pathological slices. *J Magn Reson Imaging* 2010; 32:1149–1157.
126. Jacobs MA, Windham JP, Soltanian-Zadeh H, et al. Registration and warping of magnetic resonance images to histological sections. *Med Phys* 1999; 26:1568–1578.
127. Park H, Piert MR, Khan A, et al. Registration methodology for histological sections and in vivo imaging of human prostate. *Acad Radiol* 2008; 15:1027–1039.
128. Meyer CR, Moffat BA, Kuszpit KK, et al. A methodology for registration of a histological slide and in vivo MRI volume based on optimizing mutual information. *Mol Imaging* 2006; 5:16–23.
129. Viswanath S, Bloch BN, Rosen M, et al. Integrating structural and functional imaging for computer assisted detection of prostate cancer on multi-protocol 3 Tesla MRI. *Proc Soc Photo Opt Instrum Eng* 2009; 7260:72603I.
130. Gibson E, Gaed M, Gomez JA, et al. 3D prostate histology image reconstruction: quantifying the impact of tissue deformation and histology section location. *J Pathol Inform* 2013; 4:31.
131. Gibson E, Gaed M, Gomez JA, et al. 3D prostate histology reconstruction: an evaluation of image-based and fiducial-based algorithms. *Med Phys* 2013; 40:093501.
132. Patel P, Chappelow J, Tomaszewski J, et al. Spatially weighted mutual information (SWMI) for registration of digitally reconstructed ex vivo whole mount histology and in vivo prostate MRI. *Conf Proc IEEE Eng Med Biol Soc* 2011; 2011:6269–6272.
133. McGrath DM, Vlad RM, Foltz WD, et al. Technical note: fiducial markers for correlation of whole-specimen histopathology with MR imaging at 7 tesla. *Med Phys* 2010; 37:2321–2328.
134. Toth RJ, Shih N, Tomaszewski JE, et al. Histostitcher: an informatics software platform for reconstructing whole-mount prostate histology using the extensible imaging platform framework. *J Pathol Inform* 2014; 5:8.
135. Chappelow J, Bloch BN, Rofsky N, et al. Elastic registration of multimodal prostate MRI and histology via multiattribute combined mutual information. *Med Phys* 2011; 38:2005–2018.
136. Orczyk C, Rusinek H, Rosenkrantz AB, et al. Preliminary experience with a novel method of three-dimensional co-registration of prostate cancer digital histology and in vivo multiparametric MRI. *Clin Radiol* 2013; 68:e652–e658.
137. Lv D, Guo X, Wang X, et al. Computerized characterization of prostate cancer by fractal analysis in MR images. *J Magn Reson Imaging* 2009; 30:161–168.
138. Rouviere O, Papillard M, Girouin N, et al. Is it possible to model the risk of malignancy of focal abnormalities found at prostate multiparametric MRI? *Eur Radiol* 2012; 22:1149–1157.
139. Meyer C, Ma B, Kunju LP, et al. Challenges in accurate registration of 3-D medical imaging and histopathology in primary prostate cancer. *Eur J Nucl Med Mol Imaging* 2013; 40:72–78.
140. Viswanath S, Bloch BN, Genega E, et al. A comprehensive segmentation, registration, and cancer detection scheme on 3 Tesla in vivo prostate DCE-MRI. *Med Image Comput Comput Assist Interv* 2008; 11:662–669.
141. Liu X, Langer DL, Haider MA, et al. Prostate cancer segmentation with simultaneous estimation of Markov random field parameters and class. *IEEE Trans Med Imaging* 2009; 28:906–915.
142. Artan Y, Haider MA, Langer DL, et al. Prostate cancer localization with multispectral MRI using cost-sensitive support vector machines and conditional random fields. *IEEE Trans Image Process* 2010; 19:2444–2455.
143. Vos PC, Hambrook T, Barentsz JO, et al. Computer-assisted analysis of peripheral zone prostate lesions using T2-weighted and dynamic contrast enhanced T1-weighted MRI. *Phys Med Biol* 2010; 55:1719–1734.
144. Viswanath S, Bloch BN, Chappelow J, et al. Enhanced multi-protocol analysis via intelligent supervised embedding (EMPrAVISE): detecting prostate cancer on multi-parametric MRI. *Proc SPIE Int Soc Opt Eng* 2011; 7963:79630u.
145. Lopes R, Ayache A, Makni N, et al. Prostate cancer characterization on MR images using fractal features. *Med Phys* 2011; 38:83–95.
146. Sung YS, Kwon HJ, Park BW, et al. Prostate cancer detection on dynamic contrast-enhanced MRI: computer-aided diagnosis versus single perfusion parameter maps. *AJR Am J Roentgenol* 2011; 197:1122–1129.
147. Artan Y, Yetik IS. Prostate cancer localization using multiparametric MRI based on semi-supervised techniques with automated seed initialization. *IEEE Trans Inf Technol Biomed* 2012; 16:1313–1323.
148. Tiwari P, Kurhanewicz J, Madabhushi A. Multi-kernel graph embedding for detection, Gleason grading of prostate cancer via MRI/MRS. *Med Image Anal* 2013; 17:219–235.
149. Ginsburg SB, Viswanath SE, Bloch BN, et al. Novel PCA-VIP scheme for ranking MRI protocols and identifying computer-extracted MRI measurements associated with central gland and peripheral zone prostate tumors. *J Magn Reson Imaging* 2015; 41:1383–1393.
150. Niaf E, Flamary R, Rouviere O, et al. Kernel-based learning from both qualitative and quantitative labels: application to prostate cancer diagnosis based on multiparametric MR imaging. *IEEE Trans Image Process* 2014; 23:979–991.

151. Zhao K, Wang C, Hu J, et al. Prostate cancer identification: quantitative analysis of T2-weighted MR images based on a back propagation artificial neural network model. *Sci China Life Sci* 2015; 58:666–673.
152. Saman DM, Lemieux AM, Nawal Lutfiyya M, et al. A review of the current epidemiology and treatment options for prostate cancer. *Dis Mon* 2014; 60:150–154.
153. Keyes M, Crook J, Morton G, et al. Treatment options for localized prostate cancer. *Can Fam Physician* 2013; 59:1269–1274.
154. Oto A, Yang C, Kayhan A, et al. Diffusion-weighted and dynamic contrast-enhanced MRI of prostate cancer: correlation of quantitative MR parameters with Gleason score and tumor angiogenesis. *AJR Am J Roentgenol* 2011; 197:1382–1390.
155. Anwar SS, Anwar Khan Z, Shoaib Hamid R, et al. Assessment of apparent diffusion coefficient values as predictor of aggressiveness in peripheral zone prostate cancer: comparison with Gleason score. *ISRN Radiol* 2014; 2014:263417.
156. Hambrock T, Somford DM, Huisman HJ, et al. Relationship between apparent diffusion coefficients at 3.0-T MR imaging and Gleason grade in peripheral zone prostate cancer. *Radiology* 2011; 259:453–461.
157. Yamamura J, Salomon G, Buchert R, et al. MR imaging of prostate cancer: diffusion weighted imaging and (3D) hydrogen 1 (H) MR spectroscopy in comparison with histology. *Radiol Res Pract* 2011; 2011:616852.
158. Gibbs P, Liney GP, Pickles MD, et al. Correlation of ADC and T2 measurements with cell density in prostate cancer at 3.0 Tesla. *Invest Radiol* 2009; 44:572–576.
159. Anderson AW, Xie J, Pizzonia J, et al. Effects of cell volume fraction changes on apparent diffusion in human cells. *Magn Reson Imaging* 2000; 18:689–695.
160. Tanimoto K, Yoshikawa K, Obata T, et al. Role of glucose metabolism and cellularity for tumor malignancy evaluation using FDG-PET/CT and MRI. *Nucl Med Commun* 2010; 31:604–609.
161. Kobus T, Hambrock T, Hulsbergen-van de Kaa CA, et al. In vivo assessment of prostate cancer aggressiveness using magnetic resonance spectroscopic imaging at 3 T with an endorectal coil. *Eur Urol* 2011; 60:1074–1080.
162. Zakian KL, Sircar K, Hricak H, et al. Correlation of proton MR spectroscopic imaging with Gleason score based on step-section pathologic analysis after radical prostatectomy. *Radiology* 2005; 234:804–814.
163. van Asten JJ, Cuijpers V, Hulsbergen-van de Kaa C, et al. High resolution magic angle spinning NMR spectroscopy for metabolic assessment of cancer presence and Gleason score in human prostate needle biopsies. *MAGMA* 2008; 21:435–442.
164. Garcia-Martin ML, Adrados M, Ortega MP, et al. Quantitative (1) H MR spectroscopic imaging of the prostate gland using LCMoDel and a dedicated basis-set: correlation with histologic findings. *Magn Reson Med* 2011; 65:329–339.
165. Scheenen TW, Heijmink SW, Roell SA, et al. Three-dimensional proton MR spectroscopy of human prostate at 3 T without endorectal coil: feasibility. *Radiology* 2007; 245:507–516.
166. Shukla-Dave A, Hricak H, Ishill NM, et al. Correlation of MR imaging and MR spectroscopic imaging findings with Ki-67, phospho-Akt, and androgen receptor expression in prostate cancer. *Radiology* 2009; 250:803–812.
167. Lee DH, Koo KC, Lee SH, et al. Tumor lesion diameter on diffusion weighted magnetic resonance imaging could help predict insignificant prostate cancer in patients eligible for active surveillance: preliminary analysis. *J Urol* 2013; 190:1213–1217.
168. Epstein JI, Allsbrook WC, Jr, Amin MB, et al. The 2005 International Society of Urological Pathology (ISUP) consensus conference on Gleason grading of prostatic carcinoma. *Am J Surg Pathol* 2005; 29:1228–1242.
169. Cam K, Yucel S, Turkeri L, et al. Accuracy of transrectal ultrasound guided prostate biopsy: histopathological correlation to matched prostatectomy specimens. *Int J Urol* 2002; 9:257–260.
170. Quann P, Jarrard DF, Huang W. Current prostate biopsy protocols cannot reliably identify patients for focal therapy: correlation of low-risk prostate cancer on biopsy with radical prostatectomy findings. *Int J Clin Exp Pathol* 2010; 3:401–407.
171. Djavan B, Ravery V, Zlotta A, et al. Prospective evaluation of prostate cancer detected on biopsies 1, 2, 3 and 4: when should we stop? *J Urol* 2001; 166:1679–1683.
172. Futterer JJ, Barentsz JO. MRI-guided and robotic-assisted prostate biopsy. *Curr Opin Urol* 2012; 22:316–319.
173. Moore CM, Robertson NL, Arsanious N, et al. Image-guided prostate biopsy using magnetic resonance imaging-derived targets: a systematic review. *Eur Urol* 2013; 63:125–140.
174. Xu H, Lasso A, Guion P, et al. Accuracy analysis in MRI-guided robotic prostate biopsy. *Int J Comput Assist Radiol Surg* 2013; 8:937–944.
175. Zamecnik P, Schouten MG, Krafft AJ, et al. Automated real-time needle-guide tracking for fast 3-T MR-guided transrectal prostate biopsy: a feasibility study. *Radiology* 2014; 273:879–886.
176. Fiard G, Hohn N, Descotes JL, et al. Targeted MRI-guided prostate biopsies for the detection of prostate cancer: initial clinical experience with real-time 3-dimensional transrectal ultrasound guidance and magnetic resonance/transrectal ultrasound image fusion. *Urology* 2013; 81:1372–1378.
177. Xu S, Kruecker J, Turkbey B, et al. Real-time MRI-TRUS fusion for guidance of targeted prostate biopsies. *Comput Aided Surg* 2008; 13:255–264.
178. Mitra J, Ghose S, Sidibe D, et al. Joint probability of shape and image similarities to retrieve 2D TRUS-MR slice correspondence for prostate biopsy. *Conf Proc IEEE Eng Med Biol Soc* 2012; 2012:5416–5419.
179. Wang S, Burt K, Turkbey B, et al. Computer aided-diagnosis of prostate cancer on multiparametric MRI: a technical review of current research. *Biomed Res Int* 2014; 2014:789561.
180. Fei BW, Lee ZH, Boll DT, et al. Image registration and fusion for interventional MRI guided thermal ablation of the prostate cancer. In: Ellis RE, Peters TM, eds. *Medical image computing and computer-assisted intervention—MICCAI 2003, Pt 2*. Vol. 2879, Lecture Notes in Computer Science. 2003; 364–372.
181. Akbari H, Fei BW. 3D ultrasound image segmentation using wavelet support vector machines. *Med Phys* 2012; 39:2972–2984.
182. Fei BW, Lee ZH, Boll DT, et al. Registration and fusion of SPECT, high-resolution MRI, and interventional MRI for thermal ablation of prostate cancer. *IEEE Trans Nucl Sci* 2004; 51:177–183.
183. Fei BW, Lee ZH, Duerk JL, et al. Image registration for interventional MRI guided procedures: interpolation methods, similarity measurements, and applications to the prostate. In: Gee JC, Maintz JBA, Vannier MW, eds. *Biomedical image registration*. Vol. 2717, Lecture Notes in Computer Science. 2003; 321–329.
184. Fei BW, Ng WS, Chauhan S, et al. The safety issues of medical robotics. *Reliab Eng Syst Saf* 2001; 73:183–192.
185. Fei BW, Wang H, Meyers JD, et al. High-field magnetic resonance imaging of the response of human prostate cancer to Pc 4-based photodynamic therapy in an animal model. *Lasers Surg Med* 2007; 39:723–730.
186. Fei BW, Wang HS, Wu CY, et al. Choline PET for monitoring early tumor response to photodynamic therapy. *J Nucl Med* 2010; 51:130–138.
187. Fei BW, Yang XF, Nye JA, et al. MR/PET quantification tools: registration, segmentation, classification, and MR-based attenuation correction. *Med Phys* 2012; 39:6443–6454.
188. Wang HS, Fei BW. Diffusion-weighted MRI for monitoring tumor response to photodynamic therapy. *J Magn Reson Imaging* 2010; 32:409–417.
189. Wang HS, Fei BW. An MR image-guided, voxel-based partial volume correction method for PET images. *Med Phys* 2012; 39:179–194.
190. Wang HS, Fei BW. Nonrigid point registration for 2D curves and 3D surfaces and its various applications. *Phys Med Biol* 2013; 58:4315–4330.
191. Song I, Kim CK, Park BK, et al. Assessment of response to radiotherapy for prostate cancer: value of diffusion-weighted MRI at 3 T. *AJR Am J Roentgenol* 2010; 194:W477–W482.
192. Padhani AR, Makris A, Gall P, et al. Therapy monitoring of skeletal metastases with whole-body diffusion MRI. *J Magn Reson Imaging* 2014; 39:1049–1078.
193. Graham TJ, Box G, Tunariu N, et al. Preclinical evaluation of imaging biomarkers for prostate cancer bone metastasis and response to cabozantinib. *J Natl Cancer Inst* 2014; 106:dju033.
194. Lee KC, Bradley DA, Hussain M, et al. A feasibility study evaluating the functional diffusion map as a predictive imaging biomarker for detection of treatment response in a patient with metastatic prostate cancer to the bone. *Neoplasia* 2007; 9:1003–1011.
195. Sosna J, Pedrosa I, Dewolf WC, et al. MR imaging of the prostate at 3 Tesla: comparison of an external phased-array coil to imaging with an endorectal coil at 1.5 Tesla. *Acad Radiol* 2004; 11:857–862.

196. Turkbey B, Merino MJ, Gallardo EC, et al. Comparison of endorectal coil and nonendorectal coil T2W and diffusion-weighted MRI at 3 Tesla for localizing prostate cancer: correlation with whole-mount histopathology. *J Magn Reson Imaging* 2014; 39:1443–1448.
197. Litjens GJ, Barentsz JO, Karssemeijer N, et al. Clinical evaluation of a computer-aided diagnosis system for determining cancer aggressiveness in prostate MRI. *Eur Radiol* 2015; 25:3187–3199.
198. Matulewicz L, Jansen JF, Bokacheva L, et al. Anatomic segmentation improves prostate cancer detection with artificial neural networks analysis of 1H magnetic resonance spectroscopic imaging. *J Magn Reson Imaging* 2014; 40:1414–1421.
199. Huang PW, Lee CH. Automatic classification for pathological prostate images based on fractal analysis. *IEEE Trans Med Imaging* 2009; 28:1037–1050.
200. Sonn GA, Margolis DJ, Marks LS. Target detection: magnetic resonance imaging-ultrasound fusion-guided prostate biopsy. *Urol Oncol* 2014; 32:903–911.